UCLouvain

École polytechnique de Louvain

OACTIV-27: Bio-sourced Activated Carbon Production for PFAS/TFA Removal from Water, Process Design and Thermal Modelling of a Pilot-Scale Fixed-Bed Kiln

Author: **Jordi Mundet i Figueras**
Supervisor: **Hervé Jeanmart**
Readers: **Nicolas Parmentier, Patrick Gerin**
Academic year 2025 – 2026
Master [120] in Mechanical Engineering

Abstract

Per- and polyfluoroalkyl substances (PFAS), and in particular the short-chain trifluoroacetate (TFA), are difficult to remove from drinking water because they are chemically very stable and highly mobile in the aqueous phase. Granular activated carbon (GAC) is one of the most widely used technologies to capture them, and bio-sourced feedstocks can reach the specific surface areas needed for the application (above 1200 m^2/g) if they receive the right treatment. This work covers the design and thermal modelling of a fixed-bed kiln producing activated carbon from Belgian hardwood biomass, through a two-step process combining slow pyrolysis and physical steam activation. The thermal model is coupled to the CRECK 2020-03 pyrolysis kinetics to predict the biomass and structural temperatures, and the SPY code is adapted to describe the macroscopic behaviour of a single biomass particle during both the pyrolysis and the activation phases. The prototype is sized for a laboratory environment, so that the main modelling hypotheses can be tested experimentally.

1 Introduction

1.1 PFAS Contamination and Activated Carbon Treatment

Per- and polyfluoroalkyl substances (PFAS) are a family of roughly 10,000 synthetic chemicals [1]. They are water-resistant, stain-resistant and non-stick, which is why they have ended up in such a wide range of everyday and industrial products. Their production, use and disposal have released PFAS into air, soil and water [2], and the same chemical robustness that made them attractive in the first place is what makes them persist in the environment afterwards [2]. The scale of drinking-water contamination has now triggered regulatory limits, including the US EPA's 2024 Maximum Contaminant Levels (MCLs) of 4 ng/L for PFOA and PFOS [3].

Granular activated carbon (GAC) is one of the technologies used to remove PFAS from water. It is a porous solid with a very high internal surface area, produced from feedstocks such as lignite coal, peat, wood or coconut shells. Physical or chemical treatments are applied to the raw material to create and enlarge the pore network, which is what gives the final carbon its high surface area per mass unit [4]. In a treatment plant, the contaminated water is pushed through columns packed with GAC, and dissolved species are retained on the internal surfaces of the pores. For PFAS specifically, the retention is mainly driven by hydrophobic and electrostatic interactions between the molecule and the pore wall [5].

The carbon does not adsorb indefinitely. Once the available surface is saturated, PFAS molecules start passing through unretained, which is the *breakthrough* shown on the right of Fig. 1. When the outlet concentration exceeds the regulatory limit, the column is considered spent and has to be replaced with virgin or reactivated carbon. The time between two replacements is the so-called bed life, usually reported in bed volumes of water treated [4].

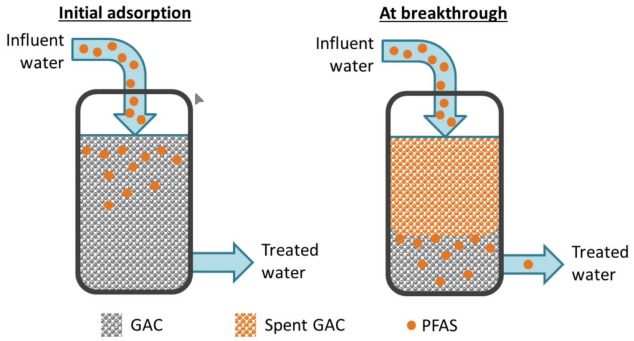

Figure 1: Conceptual diagram of the GAC treatment process showing initial adsorption (left) and breakthrough (right). Adapted from US EPA 815R24011.

There are many different ways to use GAC, the one represented in Fig 1 is one of the most common.

The US EPA lists GAC as a Best Available Technology (BAT) for PFAS removal [4], and full-scale drinking-water plants confirm that it works in practice. The method still has limitations: reactivating spent GAC destroys 10 to 30 % of the material, the fate of the PFAS during reactivation is not fully understood, and there are open questions about air emissions and waste classification. Capital costs are also high, which is a real barrier for the smallest water systems.

The OACTIV-27 project targets a bio-sourced activated carbon, made from Belgian hardwood biomass, that meets the following specifications: BET surface area $\geq$ 1200 m^2/g, micropore volume $V_{mi} \geq 0.45$ cm^3/g, adsorption kinetics $t_{90} \leq 5$ min, ash content below 5 %, and a cylindrical extruded form of 3 to 5 mm in diameter [6]. These specifications are chosen to give a product that is effective on PFAS while keeping the production route simple, since physical steam activation alone is enough to reach them.

1.2 Lignocellulosic Biomass and Pyrolysis Mechanisms

Lignocellulosic biomass consists of three primary natural polymers: cellulose (35 to 50%), hemicellulose (25 to 35%), and lignin (20 to 35%) [7–9]. Their relative proportions and thermal behaviour dictate the final properties of the activated carbon precursor [10]. Hardwoods typically exhibit balanced compositions that are ideal for this process, as high-lignin feedstocks are particularly valued for their propensity to form stable, dense char during thermal decomposition [9, 11].

The three components decompose at different stages during heating:

- **Hemicellulose** is the most thermally sensitive, breaking down rapidly between 200°C and 350°C [7, 12]. It contributes significantly to the production of light gases and pyrolytic vapours but yields very little solid char.
- **Cellulose** decomposes sharply between 300°C and 400°C. While it provides the structural framework of

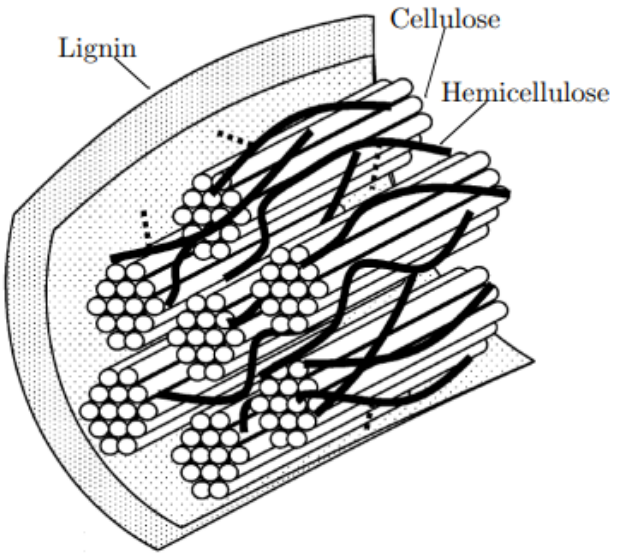

Figure 2: Structure of lignocellulosic biomass: cellulose, hemicellulose and lignin [7].

the biomass, it transforms primarily into condensable tars (bio-oil) and gases during pyrolysis [7, 9, 12].

- **Lignin** is the most heat-resistant component, decomposing slowly across a wide temperature range (160°C to 600°C) [12]. It is the key "char-former" of the biomass; its aromatic rings rearrange to form the carbon-rich solid matrix (biochar) that will later be developed into a porous structure during activation [9–12].

The pyrolysis mechanism occurs through three distinct physical stages [7, 8, 12]:

1. **Drying and Initial Depolymerisation (<250°C)**: Evaporation of bound water and the first breakages of weak chemical bonds in hemicellulose [7, 8, 12], this process is endothermic and an external source of energy is needed.

2. **Primary Pyrolysis (250–400°C)**: Major mass loss where polymers break into volatiles and the initial solid char structure forms [7, 9, 12], this process is highly exothermic.

3. **Secondary Pyrolysis (>400°C)**: Cracking of heavy vapours within the pores of "thermally thick" particles, leading to secondary char formation and the release of light gases like H_2 and CH_4 [7, 8, 12, 13], in this phase there is no longer a production of high energy gases, we thus need an external source of energy.

The end product due to pyrolysis (see Fig. 3) produces three things: **solid biochar** (30%), **liquid bio-oil** (40%), and **non-condensable syngas** (30%). The yields are highly sensitive to the pyrolysis regime (Table 1).

The OACTIV-27 protocol utilises slow pyrolysis reaching 400°C with a controlled heating rate of 2.2°C/min. This specific regime is selected to maximise the char yield,

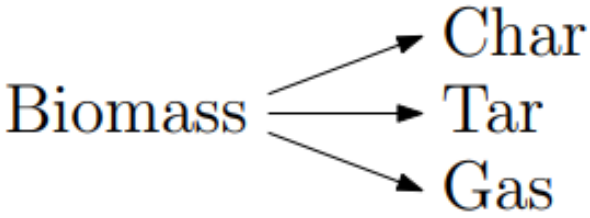

Figure 3: Biomass decomposition after pyrolysis.

Table 1: Pyrolysis regimes and typical product yields [8, 9, 12].

Type	T (°C)	Heating Rate	Biochar Yield (%)
Torrefaction	200-300	1-5°C/min	70-85
Slow Pyrolysis	**400-600**	**5-15°C/min**	**25-35**
Fast Pyrolysis	450-550	>100°C/s	10-15
Gasification	700-1200	Variable	<10

that can be utilised during the activation phase to augment the specific surface to the desired limit.

1.3 Activation Methods: Physical and Chemical Routes

The biochar produced by slow pyrolysis inherits the cellular morphology of the original biomass, but its specific surface area remains low, typically a few tens of m^2/g, because most of the pore network is partially blocked by heavy tars and incomplete decomposition residues that condense inside the pores during cooling [14]. The role of the activation step is to remove these obstructions and enlarge the existing porosity, raising the adsorption surface by one to two orders of magnitude through the controlled gasification of roughly half of the carbon mass [10].

Two routes are used in practice. **Physical activation** exposes the biochar to steam or CO_2 at 700–1050 °C, where the water–gas reaction $C + H_2O \rightarrow CO + H_2$ (or the analogous reaction for CO_2) selectively oxidises amorphous carbon and clears the pore channels [10, 12]. CO_2 is sometimes preferred to steam for its lower reactivity, which makes the process easier to control and yields a more uniform microporosity [14]. **Chemical activation** instead impregnates the biomass or biochar with a dehydrating or alkaline agent, typically KOH, $ZnCl_2$, H_3PO_4 or K_2CO_3, before heating to 400–950 °C, depending on the agent [10, 12, 14].

The trade-off between the two methods is essentially a balance between performance and process simplicity. Chemical activation reaches higher surface areas more reliably: [14] report 1194 m^2/g on KOH-activated waste wood, against only 249 and 385 m^2/g for the same biochar treated with steam and CO_2 respectively, and KOH can in principle approach the theoretical limit of graphene at about 2600 m^2/g [10]. The downside is operational: impregnation, agent recovery and post-activation washing add steps, generate contaminated effluents and require corrosion-resistant equipment [14]. Physical activation, in contrast, needs only water as a reactant and produces no chemical waste stream, at the price of a somewhat

lower surface area for a given burn-off; its efficiency drops markedly for ash-rich feedstocks because inorganic compounds tend to block the pore entrances [15], but the Belgian hardwoods used in OACTIV-27 stay below a 5 % of ash, which keeps the steam route both technically viable and operationally simple. Steam activation is therefore the method adopted in the rest of this work.

1.4 Steam Activation and Pore Development

Steam/physical activation consists of a controlled partial gasification of biochar at high temperatures, typically ranging from 700°C to 900°C, under a steam-rich atmosphere [10, 12, 14]. The process is primarily driven by the endothermic water-gas reaction, which consumes carbon from the solid matrix to produce carbon monoxide and hydrogen:

$$C(s) + H_2O(g) \rightarrow CO(g) + H_2(g)$$

Due to the strongly endothermic nature of this reaction, a continuous and significant heat input from the burner is required throughout the activation plateau to sustain the process [10, 12, 14].

The mechanism of pore development relies on the selective oxidation of carbon atoms. Steam reacts preferentially with amorphous carbon regions and reactive sites, clearing channels that were previously blocked by heavy tars during the pyrolysis phase [10, 14]. This structural evolution is essential to achieve the OACTIV-27 performance specifications: a BET surface area $\geq$ 1200 m^2/g and a micropore volume $V_{mi} \geq 0.45$ cm^3/g. These characteristics are necessary to ensure the efficient capture of PFAS and TFA molecules through hydrophobic and electrostatic interactions [5, 14].

The efficiency of pore creation is governed by "burn-off," which represents the percentage of carbon mass lost during activation [12]. For hardwood biochars, the internal surface area typically increases until a peak is reached at 35–45% burn-off, beyond which the walls between pores may collapse, leading to a decrease in adsorption capacity [10, 12, 14]. The typical evolution of biochar properties during steam activation of hardwood biochar at 800°C with an oxidant/carbon ratio of approximately 2.08 is summarised in Table 2.

Table 2: Evolution of biochar properties during steam activation of hardwood biochar at 800°C with H_2O/C ratio $\approx$ 2.08 [12].

Duration (min)	BET (m^2/g)	Burn-off (%)
120	617	45.5
210	793	47.9
300	980	64.0

The OACTIV-27 protocol adopts an activation time of 240 to 300 minutes at 800°C to reach the target surface area while maintaining the mechanical strength required for extruded cylindrical pellets.

1.5 Industrial Kiln Technologies

The choice of a kiln for activated carbon depends on different parameters such as the throughput, atmosphere control, mechanical reliability and optimisation and the user of such machines. In the industry, four primary configurations are used to handle these thermal processes: rotary kilns, screw reactors, fixed-bed batch reactors, and multiple hearth furnaces.

1.5.1 Overview of Industrial Technologies

Rotary kilns are the most common for high-volume production. They consist of an inclined rotating drum where material moves by gravity. While they handle various feedstocks well, their mechanical complexity (rotating seals at 800°C) makes them difficult to maintain and seal for precise atmospheres.

Screw reactors use a rotating screw inside a heated tube to transport biomass. They offer a compact design and good residence time control, but the friction between the screw and the biomass often leads to pellet *attrition*, breaking the particles into dust.

Multiple hearth furnaces are vertically stacked circular hearths where material moves downward through different temperature zones [16]. This is the "gold standard" for industrial scale, allowing drying, pyrolysis, and activation in one pass, but the massive capital cost and size make them unsuitable for a pilot project [16].

Fixed-bed batch reactors are stationary chambers where the biomass is heated in batches. This is the simplest design, with no moving parts at high temperature, which ensures excellent atmosphere control and keeps the pellets intact [17].

1.6 The OACTIV-27 Project and Production Protocol

1.6.1 Project Context and Partnership

The OACTIV-27 project is a Belgian collaborative initiative, bringing together three partners: CRA-W (Walloon Agricultural Research Center) leads biomass sourcing and characterisation, UCLouvain (EPL) develops pyrolysis and activation processes with associated thermal modelling, and Fours H&C contributes industrial kiln engineering and prototype fabrication.

The objective is producing bio-sourced activated carbon from locally-available Belgian biomass specifically tailored for PFAS and TFA removal from drinking water creating a **cylindrical fixed-bed batch reactor that is easy to transport and use**. with two product forms:

- Extruded cylindrical sticks exhibiting rapid adsorption kinetics (t_{90} less than or equal to 5 min) for packed-bed filtration systems
- Fine granules (0.2 to 0.6 mm) for tea-bag-style point-of-use applications

KPIs include BET surface area greater than or equal to 1200 m^2/g, micropore volume greater than or equal to 0.45 cm^3/g according to OACTIV-27 specifications.

1.6.2 Objectives for this article

The objectives for this article include:

- **Process proposal:** Propose a plan for a lab prototype of a fixed-bed kiln that is easy to use and transport and its equipment.
- **Energy Recovery:** Developing an afterburner system to recover heat from pyrolysis gases, improving the overall energy efficiency of the process.
- **Formulating coupled ordinary differential equations**: for biomass and structural temperatures incorporating CRECK 2020-03 reaction enthalpies, convective heat transfer from flue gases, thermal capacity evolution, and external heat losses
- **Coupling SPY prediction model**: associate the SPY simulation of a particle of biomass to the thermal model of the prototype.
- **Material Specification:** Selecting high-performance materials capable of surviving the 800°C steam-rich environment.
- **Quantifying energy consumption and production:** Quantify burner power requirements, propane consumption, Losses and energy production.

In short, this work proposes the design of a prototype kiln and its thermal model that predicts temperature evolution, energy requirements, and combustible consumption.

1.7 Article Structure

The article is structured as follows:

- **Section 2** presents materials and methods including the production protocol, reactor geometry, thermal model formulation and SPY simulation protocols.
- **Section 3** reports results on temperature profiles, energy balances, and burner sizing.
- **Section 4** discusses implications of the results and their impact on the equipment.
- **Section 5** concludes with recommendations for prototype fabrication and experimental validation.

2 Materials and Methods

2.1 Two-Step Production Protocol

To attain the objective of the project we proposed a two-step protocol, thus separating the pyrolysis and the activation of the biomass. The idea of the protocol is the following: having two parallel kilns one doing the pyrolysis and the other doing the activation and the two of them being heated with an external combustion chamber.(Fig 4).

The heating rate is going to be set at 2.2°C/min because:

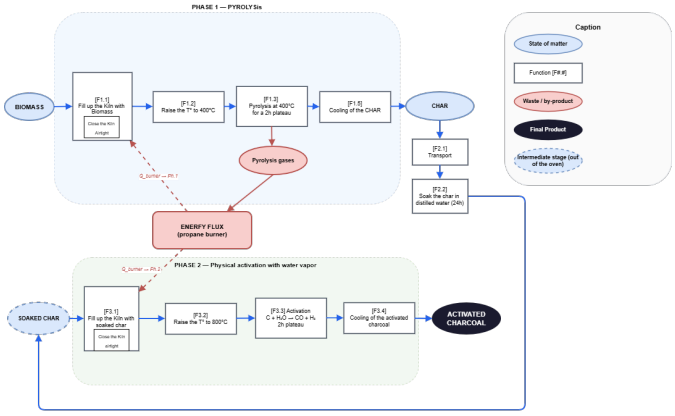

Figure 4: Function structure of the 2 step production prototype

1. **Slow pyrolysis improves biochar yield**, the lower heating rates favour char-forming reactions.
2. **Reduced thermal stress on refractory materials**, the lower heating rates decrease thermal shock risk and extend refractory service life
3. **More uniform temperature distribution**, the slower heating rates allow better radial equilibration within the biomass bed, minimising centre-to-surface gradients [9] .

This two-furnace approach (pyrolysis → unload → impregnate → reload → activate) enables self-sufficient steam generation: water pre-loaded into biochar pores during the 24-h soaking step and vaporises progressively during the activation ramp to 800°C, releasing steam directly within the pore network at the reaction site. This in-situ steam delivery eliminates the need for external steam generators (boilers, superheaters, condensate treatment) and associated infrastructure.

The extended total cycle time (approximately 45 h including cooling periods) and manual biochar handling between steps is needed but it makes the process easier and more flexible (enabling independent optimisation of pyrolysis and activation conditions), and reduced capital investment.

2.2 Reactor Thermal Model Overview

The reactor-scale thermal model has been developed to couple the kinetics of the particle of biomass undergoing pyrolysis to the dimensioning of the kiln, thus helping to determine the burner sizing, energy recovery, and operational strategy. While SPY (Section 2.3) resolves the intricate physical and chemical transformations occurring within individual biomass particles, the reactor model treats the batch as a lumped system exchanging heat with its surroundings through well-defined thermal resistances. This approach will allow us to determine the scale of the reusable energy (kW) from the pyrolysis gases, the scale of the burner and the control of the whole system.

2.2.1 Model Objectives and Scope

The reactor thermal model addresses three core questions:

1 Burner sizing: What is the instantaneous power requirement to drive the biomass temperature T_{bio} along a prescribed heating ramp (linear ramp plus isothermal plateau) while simultaneously heating the structural thermal mass (steel walls, refractory cement, insulation)? The model identifies the peak power demand occurring at the end of the ramp when structural losses are maximum, which dictates the burner's nominal capacity.

2 Energy recovery strategy: During pyrolysis (20 to 400°C), volatile release generates combustible gases (H_2, CO, CH_4, tars) whose lower heating value (LHV) can be used as an external fuel to improve efficiency. The model quantifies this substitution potential by coupling SPY's time-resolved volatile production rates with the reactor's instantaneous heat demand, yielding the net combustible consumption trajectory.

3 Activation phase feasibility: The 400 to 800°C activation ramp vaporises large quantities of water preloaded in biochar pores and drives the endothermic steam-carbon gasification reaction. The model verifies that continuous burner input can sustain the activation plateau despite these competing endothermic demands.

The model does *not* resolve spatial gradients within the reactor chamber. The volume of biomass is treated as a single particle with uniform temperature $T_{\text{bio}}(t)$. This approximation is justified by the relatively slow heating rate (2.2°C/min), and **Lab experiments** are going to test this hypothesis. For the dimensioning of the prototype we are looking for orders of magnitude for the limiting factors (such as the energy to provide for the pyrolysis or the reusable energy from pyrolysis gases), thus if the results of the SPY algorithm and the lab experiments concur, we can use the simulation results with a certain degree of confidence.

2.2.2 System Description and Thermal Network

The shape and function of the kiln have been determined according to an already existing machine called Biolyser [18].The Biolyser is designed to only do the pyrolysis of Biomass and reaches thus a maximum temperature of around 400 °C, and for our prototype we will adapt their design to enable the activation of the biomass. The kiln will have a cylindrical shape (50 cm Length and 25 cm radius for the lab prototype) and in fig 5. we can see a cross cut of the upper part of the kiln.

Heat flows from the flue gas (external annular channel, T_{fum}) through four resistance layers before dissipating to ambient air (T_{amb}). The losses due to the ambient air will be reduced thanks to an insulator that will be chosen following these criteria : cost of the insulator, efficiency of the insulator (we accept a max loss of around 20 %) and difficulty of construction of the insulator. Finally we chose refractory concrete with a thickness of 5 cm. The T_{struct} and T_{bio} are structural nodes that represent the overall temperature of the kiln and the biomass batch.
We have then resistances for each layer of the prototype that will be covered here below.

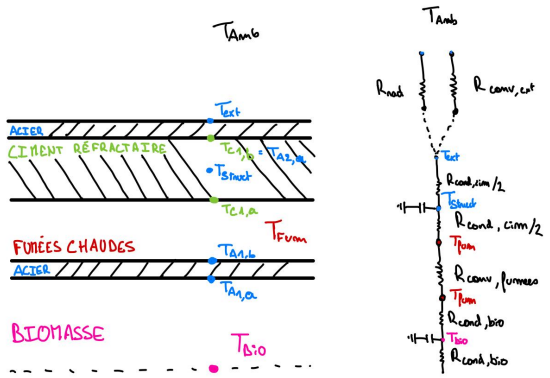

Figure 5: Cross cut of the upper part of the kiln and thermal resistances equivalent

1. **Convection from the combustion gases($R_{\text{conv,fum}}$):** Forced convection from propane combustion products circulating in the annular gap between structural layers. Typical coefficient $h_{\text{fum}} \approx 30$ W/(m^2·K).

2. **Steel conduction ($R_{\text{cond,steel}}$):** Negligible resistance (10 mm AISI 310S, $k_{\text{steel}} \approx 16$ W/(m·K)) but significant thermal capacity. As shown in the thermal resistive model, we will neglect the steel's resistances.

3. **Insulation conduction ($R_{\text{cond,iso}}$):** refractory cement (50 mm, $k_{\text{iso}} \approx 0.4$ W/(m·K)), dominant resistance contributor (59% of total R_{tot}).

4. **External losses (R_{ext}):** Parallel combination of natural convection to ambient air ($h_{\text{amb}} \approx 10$ W/(m^2·K)) and thermal radiation ($\epsilon \approx 0.8$ for oxidised steel). These resistances will have a parallel arrangement compared to the other resistances that will be in series.

5. **Bed conduction ($R_{\text{cond,biomass}}$):** packed cylindrical wood pellets ($d_p \approx 30$ mm), effective conductivity modelled as $k_{\text{eff,bed}}(T) = k_{\text{stag}} + 4\,\varepsilon_s\,\sigma\,T^3\,d_p$ combining a stagnant component derived from the wood fibre-structure model of Thunman and Leckner [19] ($k_{\text{stag}} \approx 0.15$ W/(m·K), consistent with the measurements of Guo et al. [20] on commercial wood pellets, who reported 0.146–0.192 W/(m·K)), and a radiative contribution following the Yagi–Kunii framework for packed beds [21]; radiation becomes the dominant transfer mechanism above about 400 °C and reduces $R_{\text{cond,biomass}}$ by more than an order of magnitude over the pyrolysis range.

2.2.3 Thermal Resistances and Heat Transfer Coefficients

Quantifying the thermal circuit resistances requires combining conduction through cylindrical shells, external forced convection, and parallel natural convection plus radiation. All resistances are expressed in [K/W], enabling direct Ohm's-law analogy for heat flux calculation.

2.2.4 Conduction Through Concentric Cylinders

For a cylindrical shell of inner radius R_{in}, outer radius R_{out}, length L, and thermal conductivity k, the conduction resistance is:

$$R_{\text{cond}} = \frac{\ln(R_{\text{out}}/R_{\text{in}})}{2\pi k L} \tag{1}$$

The log-mean area used in planar geometries requires:

$$A_{\text{avg}} = \frac{A_{\text{out}} - A_{\text{in}}}{\ln(A_{\text{out}}/A_{\text{in}})} \tag{2}$$

For the OACTIV-27 prototype with L= 500 mm and Radius= 250 mm, the steel layer is 10 mm thick, the refractory cement one is 50 mm thick and the annular chamber for the hot gases is 50 mm thick, this leaves 130 mm for the biomass pile. The steel resistances are negligible compared to refractories due to the 20× conductivity ratio.

2.2.5 External Forced Convection

Hot combustion products transfer heat via forced convection:

$$R_{\text{conv,fum}} = \frac{1}{h_{\text{fum}} \times A_{\text{int}}} \tag{3}$$

where $h_{\text{fum}} \approx 30$ W/(m^2·K) for turbulent gas flow.

2.2.6 External Losses, Convection and Radiation

Heat escapes via two independent mechanisms acting in parallel:

Natural convection:

$$R_{\text{rad}} = \frac{1}{h_{\text{rad}} \times A_{\text{ext,wall}}} \tag{4}$$

Thermal radiation (linearised):

$$h_{\text{rad}} = \epsilon\sigma(T_{\text{wall}} + T_{\text{amb}})(T_{\text{wall}}^2 + T_{\text{amb}}^2) \tag{5}$$

Parallel combination:

$$\frac{1}{R_{\text{ext}}} = \frac{1}{R_{\text{conv,ext}}} + \frac{1}{R_{\text{rad,ext}}} \tag{6}$$

We consider a parallel arrangement for the external resistances

2.2.7 Energy Balances Two-Node Model

The energy system has been modelled thanks to 2 ODEs that couple the temperature of the kiln (T_{struct}) and the temperature of the biomass (T_{bio}):

Node 1 Biomass: Represents the biomass batch. Temperature $T_{\text{bio}}(t)$ evolves according to:

$$\boxed{m_{\text{bio}}(t)\, c_{p,\text{bio}}(t)\, \frac{dT_{\text{bio}}}{dt} = \dot{Q}_{\text{in}} - \dot{Q}_{\text{out}} + \dot{Q}_{\text{prod}}} \tag{7}$$

$$\dot{Q}_{\text{in}} = \frac{T_{\text{fum}} - T_{\text{bio}}}{R_{\text{conv,fum}} + R_{\text{cond,biomass}}} \tag{8}$$

$$\dot{Q}_{\text{out}} = \frac{T_{\text{fum}} - T_{\text{struct}}}{R_{\text{cond,st2}} + R_{\text{cond,iso}} + R_{\text{conv,fum}}} \tag{9}$$

$$c_{p,bio}(t) = (1 - X_{char}(t)) \cdot c_{p,wood} + X_{char}(t) \cdot c_{p,char} \tag{10}$$

$$m_{bio}(t) = m_0 - \int_0^t \dot{m}_{\text{vol}}(\tau)\, d\tau \tag{11}$$

where $X_{char}(t) = \frac{m_{char}(t)}{m_0}$ is the char mass fraction relative to the initial biomass, $\dot{Q}_{\text{in}}$ is heat flux from flue gas, $\dot{Q}_{\text{out}}$ is heat flux to structural node, and $\dot{Q}_{\text{prod}}$ is the net chemical heat release provided by SPY. This term is going to be positive (exothermic reaction) when the pyrolysis gases are released and negative (endothermic reaction) before the pyrolysis starts. This term is obtained thanks to the SPY simulation.

This equation is going to be useful once the real prototype is built and the experiments start. By solving it, we can obtain the biomass temperature thanks to other parameters that can be measured such as T_{struct} and T_{fum}. For the dimensioning of the prototype we will use mostly the second ODE coupled with SPY to determine the losses and the size of the burner.

Node 2, Structure: Represents the outer kiln wall (external face of the refractory cement at radius R_5) as a lumped node with temperature $T_{\text{struct}}(t)$, comprising the outer steel jacket and the cement insulation. The inner steel wall is in thermal contact with the biomass and follows T_{bio} instead, with its sensible heat treated separately:

$$C_{\text{struct}}\, \frac{dT_{\text{struct}}}{dt} = \dot{Q}_{\text{out}} - \dot{Q}_{\text{loss}} \tag{12}$$

$$\dot{Q}_{\text{loss}}(T_{\text{struct}}) = \frac{T_{\text{struct}} - T_{\text{amb}}}{R_{\text{ext}}(T_{\text{struct}})} \tag{13}$$

The thermal capacity of the structural node is:

$$C_{\text{struct}} = m_{\text{st2}}\, c_{p,\text{st}} + m_{\text{iso}}\, c_{p,\text{iso}} \tag{14}$$

$$C_{\text{st1}} = m_{\text{st1}}\, c_{p,\text{st}} \tag{15}$$

Each cylindrical shell mass is:

$$m = \rho \cdot \pi \left(R_{\text{ext}}^2 - R_{\text{int}}^2\right) \cdot L \tag{16}$$

where $\dot{Q}_{\text{out}}$ is heat flux from biomass node and $\dot{Q}_{\text{loss}}$ is heat loss to ambient .

By solving this ODE we can find T_{struct}, and thanks to T_{struct}, we can obtain the losses of our kiln. We also take into account the thermal inertia which delays temperature increase of the biomass, because our goal is to heat up the biomass, but we will inevitably heat up the structure too, thus the amount of energy needed to heat up the biomass will increase.

2.2.8 Coupling with SPY Particle Simulations

Two time-dependent quantities link the particle-scale SPY model (Section 2.3) to the reactor-scale thermal model:

1 Reaction heat release rate: SPY integrates the volumetric heat source $\dot{\omega}_h(r, z, t)$ over the particle volume to yield the net heat release for a single particle. Scaling to the batch:

$$\dot{Q}_{\text{reac,total}}(t) = N_{\text{particles}} \times \dot{Q}_{\text{reac,single}}(t) \tag{17}$$

where $N_{\text{particles}} = m_{\text{batch}}/m_{\text{particle}}$. Positive values (exothermic secondary charring around 350–400°C) reduce burner demand; negative values (endothermic polymer activation below 280°C, endothermic activation gasification above 600°C) increase it.

2 Lower heating value of volatiles: SPY also provides the instantaneous combustion energy potentially recoverable from the pyrolysis gases by summing the LHV of each species weighted by its mass flow rate.

$$\dot{Q}_{\text{LHV}}(t) = \sum_i \text{LHV}_i \cdot \dot{m}_i(t) \tag{18}$$

2.2.9 Dynamic Heat Losses and Burner Power

Total burner input must cover:

$$\dot{Q}_{\text{burner}} = \frac{\dot{Q}_{\text{sens,bio}} + \dot{Q}_{\text{sens,str}} - \dot{Q}_{\text{reac}} + \dot{Q}_{\text{loss}} - \dot{Q}_{\text{LHV}}}{\eta_{\text{burner}}} \tag{19}$$

$$\dot{Q}_{\text{sens,bio}} = m_{\text{bio}}(t)\, c_{p,\text{bio}}(t)\, \frac{dT_{\text{bio}}}{dt} \tag{20}$$

$$\dot{Q}_{\text{sens,str}} = C_{\text{struct}}\, \frac{dT_{\text{struct}}}{dt} \tag{21}$$

where $\eta_{\text{burner}} \approx 0.85$ is burner efficiency. Thanks to SPY we can estimate the heat input at each step of time during the process.

Combustible consumption:

$$\dot{m}_{\text{comb}} = \frac{\dot{Q}_{\text{burner}}}{LHV_{comb}} \tag{22}$$

2.3 SPY Simulation Protocol

2.3.1 Model Overview

Single Particle pyrolysis (SPY) is a two-dimensional transient model developed by [7] at UCLouvain to describe the thermochemical decomposition of a fibrous lignocellulosic particle under non-isothermal conditions. The code couples a detailed multi-step kinetic mechanism with a 2D physical model of a porous fibrous particle, and solves the conservation equations for energy, solid species mass, gas-phase species mass and momentum in cylindrical coordinates. Although SPY was originally written for crushed biomass combustion in utility boilers [7], its formulation makes no assumption that restricts it to small particles, and the same framework is used here for the slow pyrolysis of cm-scale wood pieces relevant to the OACTIV-27 reactor.

In the OACTIV-27 context, SPY serves three purposes: it provides the char yield and char composition as functions of pyrolysis temperature and heating rate; it gives the transient reaction heat $\dot{Q}_{reac}(t)$ that enters the biomass energy balance ODE of the reactor model; and it produces the time-resolved gas mass flow rates $\dot{m}_i(t)$ that are needed to compute the calorific contribution of the pyrolysis volatiles to the burner duty.

2.3.2 Modelling Assumptions

Four assumptions specific to the SPY simulation are made for the OACTIV-27 application. They are stated explicitly here because each one defines a limit of validity of the coupled thermal model explained before.

(A1) Particle-to-batch extrapolation. SPY simulates a single representative particle (cm scale) and the resulting global outputs $X_{char}(t)$, $\dot{Q}_{reac}(t)$ and $\dot{m}_{vol}(t)$ are extrapolated to the entire batch as a mean. This rests on the further assumption that all particles in the batch follow a similar thermal history, which is consistent with the externally-heated annular geometry of the prototype but should be checked by a sensitivity study before quantitative use. The particles in the middle of the batch will take longer to reach the desired temperature but this has been taken into account in the thermal model with the thermal resistance of the biomass.

(A2) Macroparticle regime. Taking $h_{ext} \approx 30$ W m^{-2} K^{-1} and $k_{eq,r} \approx 0.13$ W m^{-1} K^{-1}, a 15 mm radius gives Bi ≈ 3.5, which falls within the validation envelope of SPY against PYRATES (Bi between 0.5 and 3 on a ⌀ 2 cm beech sample at 850 °C, [7, ch. 4]). Operating outside this envelope, either with much smaller particles or in a markedly more aggressive heating regime, would require a separate validation effort. In our case, if we want to extrapolate our model of the particle to the whole batch we will be in a thermally thick problem Bi>10, thus real life experiments (with the prototype) have to be done to make adjustments to the SPY simulations.

(A3) Lignocellulosic composition fixed to Blondeau's beech reference. Mass fractions are taken as 48.85 % CELL, 28.47 % HCE and 22.68 % lignin, the lignin fraction being further split into 6.48 % LIGC, 8.52 % LIGH and 7.68 % LIGO. These are the values measured by [7] on the PYRATES samples. The global sensitivity of $\dot{Q}_{reac}$ to a ±10 % variation on these fractions is assumed to be below 5 %, an assumption that should itself be verified by a parametric sweep.

(A4) One-way SPY-to-reactor coupling. SPY is run once in pre-processing with a prescribed external temperature $T_{ext}(t)$ following the target ramp-and-plateau schedule. The outputs $X_{char}(t)$, $\dot{Q}_{reac}(t)$ and $\dot{m}_{vol}(t)$ are stored as lookup tables and interpolated during the reactor-scale ODE integration. No feedback from the reactor-predicted $T_{bio}(t)$ is sent back to SPY. Should the difference between T_e and T_{bio} become significant, an iteration loop would have to be added.

2.3.3 Particle-Size Regimes and Model Applicability

The CRECK 2020-03 mechanism [11] was calibrated against thermogravimetric data, that is, on particles small enough to be considered isothermal during decomposition. Whether such a kinetic scheme can be embedded in a

reactor-scale model depends on which physical regime the particle belongs to. The relevant criterion is the Biot number $\mathrm{Bi} = h_{ext}L/k_{eq}$, with h_{ext} the external heat transfer coefficient, L a characteristic dimension and k_{eq} the effective conductivity of the porous matrix. Three regimes are commonly distinguished in the pyrolysis literature [9].

For $\mathrm{Bi} < 0.1$, typically below 200–300 µm, the particle is thermally thin: internal conduction is fast enough that temperature is uniform and pyrolysis is governed by the external heating rate and the intrinsic kinetics alone. This is the implicit framework of TGA-derived schemes such as CRECK. In the intermediate range $0.1 < \mathrm{Bi} < 10$, characteristic of mm-scale particles in fluidised beds, internal gradients are no longer negligible and a moving reaction front develops, with partially overlapping drying, devolatilisation and char formation zones. For $\mathrm{Bi} > 10$, a regime reached by cm-scale particles in fixed beds, internal heat transfer becomes the rate-limiting step: the centre lags significantly behind the surface, a dense char shell coexists with a non-reacted core, and pressure gradients due to volatile release drive a convective gas flow that further cools the particle interior [9].

The CRECK kinetic constants are scale-independent: they describe the intrinsic chemistry of cellulose, hemicellulose and lignin decomposition and apply at any temperature and composition. What changes with particle size is not the chemistry but the transport context in which the chemistry takes place. SPY embeds the kinetics in a 2D transient framework that resolves the spatial gradients responsible for the macroparticle phenomenology [7], so the same chemical scheme can be used outside its original microparticle calibration range as long as the surrounding transport problem is solved.

For the OACTIV-27 application a macro-size batch of approximately 3 cm wood pieces the macroparticle regime is the relevant one (assumption A2). Taking $h_{ext} \approx 30$ W m^{-2} K^{-1} and the effective radial conductivity $k_{eq,r} \approx 0.13$ W m^{-1} K^{-1} that Blondeau's correlations predict at the apparent density and temperature of beech undergoing pyrolysis [7], a 15 mm reference radius gives $\mathrm{Bi} \approx 3.5$, which falls within the validation envelope of SPY (see Section 2.3.8). But the whole batch (20kg) will have a different behaviour and the thermally thick regime will take place, the conductive resistance in the thermal model takes some of the problem into account but In-Lab tests will be needed to fully test A2.

2.3.4 Geometry, Domain and Symmetry Assumptions

The particle is described as a finite cylinder with axisymmetric geometry, so the computational domain reduces to a half-meridian plane $0 \le r \le L_r$, $0 \le z \le L_z$ [7]. Symmetry is imposed at $r = 0$ from the cylindrical coordinate system, and additionally at $z = 0$ (the longitudinal mid-plane) to halve the computational cost. The mesh is staggered, scalar fields (T, p, solid and gas densities) are stored at cell centres and velocity components on cell faces, and refined towards the surface, where the steepest temperature and pressure gradients occur [7].

For the OACTIV-27 reference particle the initial dimensions are $R_0 = 15$ mm and $L_0 = 30$ mm, representative of the wood chunks fed to the prototype. The radial mesh uses 50 non-uniform cells with Δr ranging from 0.1 mm at the surface to 0.5 mm at the centre, and the axial mesh 100 non-uniform cells in the same range.

2.3.5 Multi-Component Solid and Gas Phases

Fresh biomass is decomposed into the seven primary constituents of the CRECK 2020-03 scheme [11]: cellulose (CELL), hemicellulose (HCE), three lignin pseudo-components based on the dominant monolignol precursor (LIGC, LIGH, LIGO), extractives (EXTR) and bound moisture. Each pseudo-component decomposes through its own set of competitive pathways, producing intermediate active species, char, condensable tars and permanent gases. The reference composition adopted for beech (*Fagus sylvatica*) follows assumption A3 and uses the values measured by [7] on the PYRATES samples: 48.85 % CELL, 28.47 % HCE and 22.68 % lignin, the lignin fraction being further split into 6.48 % LIGC, 8.52 % LIGH and 7.68 % LIGO using the elemental method of [7]; the corresponding ultimate analysis is C = 48.7 %, H = 6.04 %, O = 45.26 % (mass, dry basis).

The gas phase contains the permanent gases (H_2, CO, CO_2, CH_4, light hydrocarbons, H_2O), oxygenated intermediates and the heavier tar species relevant to the CRECK mechanism. Secondary intra-particle reactions are not included in the present configuration, in line with Blondeau's original implementation [7], since the residence time of volatiles in the particle is short for the macroparticle conditions of interest. The governing equations and the related parameters to their solving are discussed in annex B

2.3.6 Output Variables

SPY produces two categories of output, stored at different sampling rates because they have different downstream uses.

The full spatial fields, temperature $T(r, z, t)$, pressure $p(r, z, t)$, solid mass fractions for each pseudo-component, gas mass fractions and porosity, are saved every 30 s. They are used here to verify that the centre-to-surface temperature difference is consistent with the macroparticle regime expected for the OACTIV-27 conditions (typically of the order of 100 °C during the active pyrolysis window, in line with what [7] reports for similar Biot numbers).

The global integrated quantities are saved every 1 s: total particle mass $m(t)$, char mass $m_{char}(t)$, instantaneous volatile flow rate $\dot{m}_{vol}(t)$, species-resolved gas flow rates $\dot{m}_i(t)$ for the main permanent gases and tars, and the integrated reaction heat $\dot{Q}_{reac}(t)$,

$$\dot{Q}_{reac}(t) = \int_V \omega_h \, \mathrm{d}V \tag{23}$$

This last term is the link between SPY and the reactor-scale energy balance: it provides the chemical source term that appears on the right-hand side of the biomass ODE.

For the reference run (beech, 2.2 °C min^{-1} ramp to 400 °C, 120 min plateau), SPY predicts a char yield of

approximately 22.5 % on a dry basis, with the remainder split between condensable tars and permanent gases. These values are consistent with the slow-pyrolysis literature [11].

2.3.7 Lower Heating Value of the Pyrolysis Gases

The instantaneous lower heating value released by the volatiles is reconstructed from the species flow rates and the tabulated specific LHVs:

$$\dot{Q}_{LHV}(t) = \sum_i \mathrm{LHV}_i \, \dot{m}_i(t) \tag{24}$$

with $\mathrm{LHV}_{H_2} = 120$, $\mathrm{LHV}_{CO} = 10.1$, $\mathrm{LHV}_{CH_4} = 50.0$ and $\mathrm{LHV}_{C_2H_4} = 47.2$ MJ kg^{-1}, and a representative average of ~ 18 MJ kg^{-1} for the lumped tar fraction. The cumulative integral $Q_{LHV} = \int_0^{t_{end}} \dot{Q}_{LHV}\,\mathrm{d}t$ is then used in Section 3 to evaluate the share of the burner duty that can theoretically be offset by combusting the pyrolysis gases.

It must be stressed that $\dot{Q}_{LHV}$ and $\dot{Q}_{reac}$ are two different quantities. The first is the chemical energy contained in the volatiles, available only if those volatiles are fully oxidised downstream; the second is the heat absorbed or released inside the particle by the pyrolysis reactions themselves. They enter the global energy balance through different terms and must not be confused.

2.3.8 Validation Against PYRATES

SPY was validated by [7] against measurements collected in the PYRATES facility at CEA Grenoble. Two complementary sets of experiments are reported.

A non-reactive ceramic cylinder of 2 cm diameter, instrumented with up to nine thermocouples and tested at nominal furnace temperatures of 600 and 850 °C, was first used to characterise the boundary conditions of PYRATES and to verify the pure heat transfer part of the model. The agreement on the internal temperature profiles falls within the experimental uncertainty reported by CEA/LITEN, with a better match near the centre of the sample than close to the surface, where thermocouple placement is more sensitive [7].

The pyrolysis case is a 2 cm diameter beech cylinder of aspect ratio 1.5, density 630 kg m^{-3}, dried beforehand following the French norm NF EN 14774, and instrumented with two thermocouples. The Biot number for this configuration ranges from approximately 0.5 to 3 over the heating transient. SPY reproduces the internal temperature profiles, the global mass loss and the order of magnitude of gas yields, with deviations in the detailed tar speciation that are discussed in [7] and attributed to the absence of intra-particle secondary cracking in the implemented mechanism.

For the OACTIV-27 application, the relevant point is that the validation Biot range (0.5–3) brackets the operating Biot number of the reference particle (around 3.5), so the use of SPY at this scale rests on a documented numerical and experimental basis rather than on extrapolation.

2.3.9 Coupling with the Reactor Thermal Model

Three SPY outputs feed the reactor-scale ODEs.

The biomass heat capacity $c_{p,bio}(t)$ is computed from the evolving solid composition. Following the standard approximation $c_{p,bio}(t) = (1 - X_{char}(t))\, c_{p,wood} + X_{char}(t)\, c_{p,char}$, with $c_{p,wood} \approx 1750$ J kg^{-1} K^{-1} and $c_{p,char} \approx 900$ J kg^{-1} K^{-1}, the only quantity required from SPY is the char mass fraction $X_{char}(t) = m_{char}(t)/m_0$, which is part of the output.

The reaction heat $\dot{Q}_{reac}(t)$ is taken directly from the SPY output and enters the biomass ODE as a source/sink term, negative during the endothermic activation phase and turning positive during the exothermic char-forming reactions.

This approach reflects assumptions A1 and A4: all particles in the batch are taken to follow a similar thermal history and no feedback from the reactor-predicted $T_{bio}(t)$ is sent back to SPY. Both assumptions should be checked by a sensitivity study before the model is used quantitatively.

3 Results

After several simulations of the pyrolysis at different temperature rates, we settled for a rate of 2.2 °C/min of a 3 cm diameter and 3 cm length particle of beech wood. Those parameters have been chosen because the results of the simulation can be reproduced in real life in the UCLouvain and ULB labs.

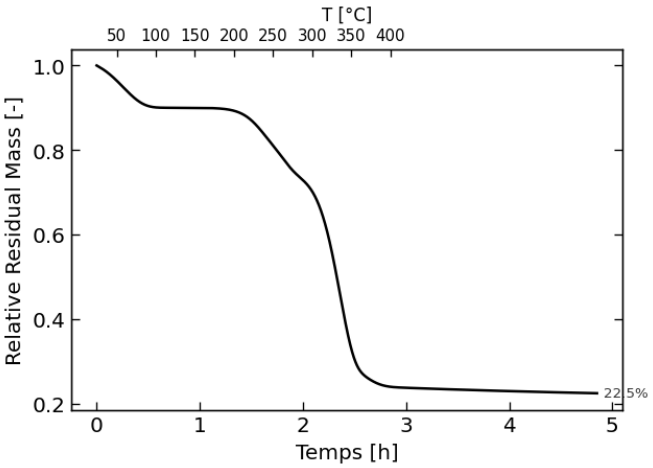

Figure 6: Char production for one beech wood particle

Figure 6 shows the relative residual mass of the particle throughout the cycle. The first small drop around 0.5 h is moisture loss, the main devolatilisation occurs from roughly 1.5 h to 2.5 h, where the curve falls steeply from 0.9 to 0.25. Between 3 h to 5 h the mass has stabilised at 22.5 %, which corresponds to the char yield under these conditions.

After the 3 h mark the curve reaches a plateau, but not quite: the temperature plateau at 400 °C slowly gasifies the char itself through secondary reactions, eroding the yield further. For a process whose objective is to maximise the carbon mass available for activation, this is an

important result. For the ideal process we should cut the burner and begin cooling once the mass plateau is reached, rather than holding the temperature for 2 h.

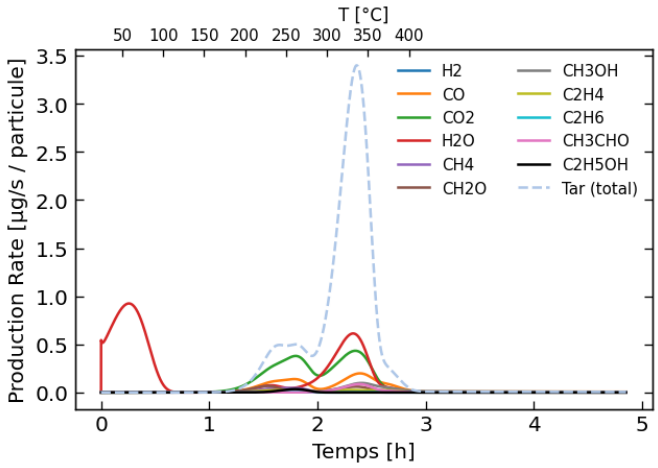

Figure 7: Production rate of pyrolysis gases and H_2O for 1 particle of beech wood

Figure 7 shows the production rates of the main volatile species for a single beech particle under the reference conditions. The first peak is water vapour only, it is entirely endothermic and ends before any devolatilisation begins. Pyrolysis starts around 200 °C and peaks near 320-350 °C, where both light gases (CO, CO_2, CH_4) and tars reach their maximum production rates before declining as the particle approaches full conversion.

What stands out is the large gap between the tar fraction (dashed line) and the permanent gases: at peak, total tar production is roughly an order of magnitude higher than any individual gas species. Most of the chemical energy leaving the particle therefore travels as condensable vapour, not as light gas. This matters directly for the afterburner: if the transfer lines between the kiln and the combustion chamber are not kept above the tar dew point, a large fraction of that energy is lost as the PAH species condenses before reaching the afterburner.

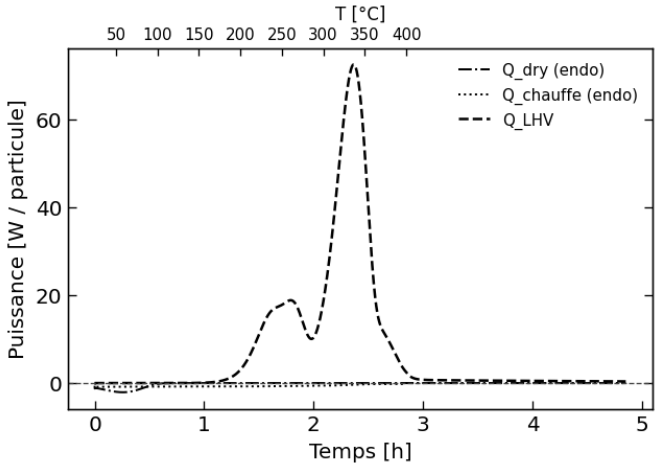

Figure 8: Energy contained in all the pyrolysis gases

Figure 8 shows the three power terms computed by SPY for a single particle. The drying heat Q_{dry} and the sensible heating $Q_{chauffe}$ are orders of magnitude inferior to the $\dot{Q}_{LHV}$, although when all the particles of the batch are taken into account their endothermic constraint becomes more relevant to the dimensioning of the combustion chamber.

The biggest term is $\dot{Q}_{LHV}$. It is defined as $\sum_i \mathrm{LHV}_i \cdot \dot{m}_i$, the sum of the combustion energies of all volatile species leaving the particle at each instant and thus, the power that the afterburner could in principle recover. It is zero for the first hour, while the polymer chains in cellulose and hemicellulose are being broken by endothermic bond scission ($Q_{chauffe}$). The burner carries the full thermal load alone during this period. The curve then rises sharply to a peak of 72.5 W particle^{-1} around 320–350 °C, where tar and gas production is at its highest, before dropping back to zero as the volatile fraction is exhausted and only char remains. Scaled to the full batch, this peak defines the maximum energy available for propane substitution and sets the upper bound on afterburner heat recovery.

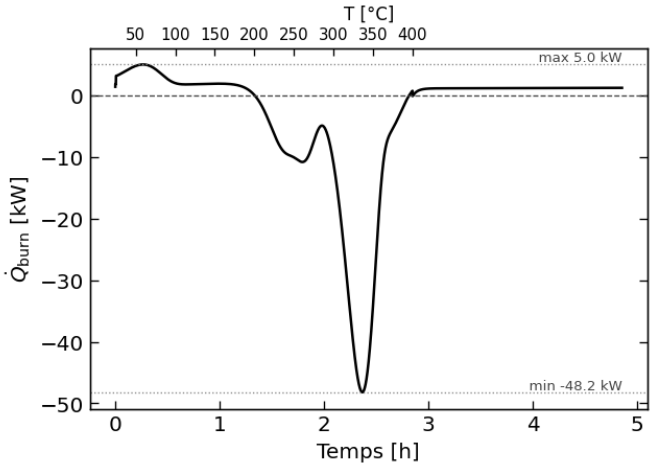

Figure 9: Energy needed from the combustion chamber

$\dot{Q}_{burn}$ is the net propane power required at each instant:

$$\dot{Q}_{burn} = \frac{\dot{Q}_{fumes} - \dot{Q}_{LHV}}{\eta_{burn}} \tag{25}$$

$\dot{Q}_{fumes}$ is itself the sum of six contributions:

$$\dot{Q}_{fumes} = \dot{Q}_{sens,bio} + \dot{Q}_{sens,str} - \dot{Q}_{reac} + \dot{Q}_{loss} \tag{26}$$

The two sensible heating terms cover the biomass and the structural node, $\dot{Q}_{reac}$ is the power needed to start the pyrolysis reaction and it is subtracted because the reaction is endothermic and finally $\dot{Q}_{loss}$ is the losses to the environment due to radiation and convection. From this total, $\dot{Q}_{LHV}$ is the energy recovered by burning the pyrolysis gases in the afterburner and it is subtracted before dividing by the burner efficiency η_{burn}. What remains is what propane must supply. Negative values on Figure 9 mean the supply comes from the burning of the pyrolysis

gases and positive means that the burner is working only with propane.

The positive peak at the start (+5 kW) does not last. It is mostly due to the evaporation of water inside the biomass, the curve remains positive until 1.5 h due to cellulose and hemicellulose decomposition the $\dot{Q}_{loss}$ term is not very large at the beginning but it will be responsible for the later stages of the demand in propane. The volatile gases surge around 1.5 h and their peak production drives the curve to −48.2 kW around 2.3 h (∼330 °C), this goes according to the production rate of pyrolysis gases (Figure 7). After 2.5 h the volatile flux collapses and the curve recovers quickly.

Beyond 3 h there are no more reactions, and the residual demand of ∼1.1 kW is entirely due to wall losses. It does not stay constant: as the heating ramp keeps the temperature of the biomass at 400 °C, T_{struct} keeps rising, the temperature difference across the outer wall grows, and $\dot{Q}_{loss} = (T_{struct} - T_{amb})/R_{ext}$ increases with it. By the end of the simulation the required power has crept up to 1.2 kW.

The values in Figure 9 are not per particle. The design of the lab prototype kiln is a cylinder of 50 cm diameter and 50 cm length; filling it to 80 % of its volume with particles identical to the simulated one gives a particle count, and every SPY output has been multiplied by that number. What the figure shows is the propane demand for one full pyrolysis cycle in the prototype.

Pyrolysis only. The activation step is not included, which matters when sizing the final burner. In the two-kiln configuration both furnaces run simultaneously, so the actual demand at any instant is $\dot{Q}_{burn,total} = \dot{Q}_{burn,pyro} + \dot{Q}_{burn,acti}$. The total curve will not be simply 2 times larger. The char soaked during the 24 h impregnation step carries 2-3× more water than the raw biomass in the pyrolysis kiln, so the opening evaporation spike in the activation cycle lands on top of the pyrolysis ramp bringing the combined demand of roughly 3-4× the +5 kW minimum seen here. And once both kilns reach steady state, the wall losses add directly: $\dot{Q}_{loss,total} = \dot{Q}_{loss,pyro} + \dot{Q}_{loss,acti}$, pushing the temperature plateau from ∼1.2 kW to roughly three times that.

4 Discussion

In this section we are going to discuss several methods for implementing the principle diagram (Figure 10) following different scenarios.

Figure 10 shows the principle diagram of the prototype proposal from the constraints and results above. The geometry is cylindrical and has been inspired by the Biolyser [18], Which is a pyrolysis kiln with some of the specifications demanded from the OACTIV-27 project.

The two-kiln architecture follows from the energy results: running pyrolysis and activation simultaneously in separate vessels means the massive volatile stream from the pyrolysis kiln is available for the self heating of the pyrolysis kiln and the activation kiln whose demands in energy are more important. Trying to do both steps in sequence in the same vessel would waste some of that energy and the physical activation method would be more difficult to implement.

Every gas outlet on both kilns goes into a single combustion chamber. Nothing is vented directly to atmosphere: pyrolysis gases, activation off-gases, and any residual volatiles during transitions all pass through the burner before leaving the system. The propane pilot sustains the chamber when the pyrolysis gas flow is too lean to be self-sustaining, once devolatilisation peaks, the recovered $\dot{Q}_{LHV}$ reduces the net propane demand to the low-power floor identified in Figure 9.

The manual charcoal extraction step between the two kilns is a deliberate simplification for easy usage and easy activation implementation.

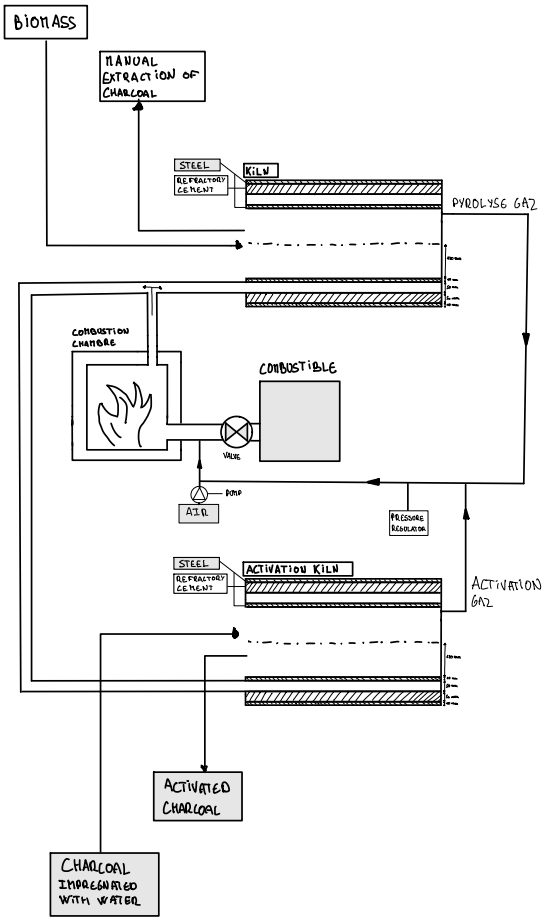

Figure 10: principle diagram of the final kiln

4.1 Thermal Oxidation of Pyrolysis Volatiles

Slow pyrolysis of biomass between 300 and 500 °C releases a heterogeneous volatile stream composed of non-condensable light gases (CO, H_2, CH_4,...) and condensable tar vapours spanning from primary oxygenated species to secondary and tertiary compounds such as toluene, benzene, and naphthalene [22]. Because all these species exit the particle in the gas phase at reactor temperature, they carry a combined LHV that can be recovered by com-

bustion. The Kinetics of the reactions pose a problem because, primary oxygenated tars begin oxidising at 650–850 K, whereas naphthalene ($C_{10}H_8$), the most refractory aromatic tar, requires temperatures above 1100 K for complete oxidation under typical excess-air conditions [23]. Designing the afterburner to destroy naphthalene therefore guarantees complete burnout of every lighter species, whose Arrhenius rate constants are larger at the same temperature [24]. They will react quicker than the heaviest tar which in this case is naphthalene. Two distinct operational scenarios are analysed below.

Case 1 , All gases burned

Operating principle. If the transfer lines between the pyrolysis chamber and the burner are held above the tar dew point, the entire volatile stream arrives at the burner in the gas phase and all its chemical energy is available for recovery. The ECN THERSITES model and experimental surveys show that raw slow-pyrolysis gas carrying Class 4–5 polycyclic aromatic hydrocarbons (PAHs) can exhibit dew points up to 190 °C [25]; consequently, transfer lines must be heat-traced to at least 250 °C with a 20–50 °C safety margin.

Case 2 , Selective condensation pathway

Operating principle. The heating of the lines that connect the kiln and the combustion chamber can be a source of inefficiency, an option to avoid this heating is to implement an intermediate condensation stage right after the release of the pyrolysis gases that collects Class 4–5 PAHs (dew points 100–190 °C, e.g. naphthalene and pyrene [25]) as a liquid fraction before they reach the afterburner. Primary and secondary oxygenated tars (phenol dew point <80 °C [26]) and all non-condensable gases remain in the vapour phase and proceed to a simpler oxidiser.

4.2 Combustion chamber technology options

The combustion chamber has to serve two functions in the same batch cycle: act as a propane furnace during ramp-up, then switch to burning the pyrolysis gases as they emerge. Four validated technologies for a combustion chamber that simultaneously burns pyrolysis gases have been identified. The differences between each technology are discussed down below and a detailed description of the operating principles of each has been described in Annex D.

Case 1 equipment: Direct-fired thermal oxidiser versus FLOX

The two most relevant architectures for OACTIV-27 are the direct-fired thermal oxidiser (DTO) and the FLOX burner. Both methods have been tested on pyrolysis gases (Tars+ Light gases).

Temperature. Standard industrial DTOs operate between 980 and 1200 °C. FLOX chambers run at 1000–1200 °C. Both architectures reach the temperature needed to burn the most refractory tar. Temperature is not the discriminating criterion.

Temperature uniformity. In a DTO, combustion is localised around the flame zone, the surrounding volume is cooler, and the temperature field is uneven. There are hot spots formation near the flame that drive NOx formation. Another implication of the uneven temperature field is the cooler peripheral zones that let refractory tar species pass through non-reacted. In FLOX there is no flame front, and oxidation is distributed homogeneously throughout the chamber volume. NOx drops below 6 ppm [27] and industrial PYREG units report >99 % PAH destruction [17].

Stability with variable LHV. A DTO sustains a localised flame, which needs a minimum fuel-air ratio to stay ignited. But in this case, the combustion chamber is made of a large refractory thermal mass that reaches temperatures up to 1000 °C and this mitigates the effect of the variable excess air ratio compared to a conventional premix burner. The hot walls act as a permanent ignition source [28]. FLOX does not have this exposure at all. Stability depends only on the chamber temperature exceeding the auto-ignition threshold everywhere in the volume [29], and that condition is set once by the propane ramp-up, not by the instantaneous gas composition.

Air supply control. Both architectures need $\lambda = 1.3$–1.6 to keep a non-zero residual O_2 throughout the residence time [30]. In a DTO with a conventional burner, the air ratio must track the gas composition in real time to keep the flame stable. In a DTO with a large refractory thermal mass, this is less critical than for a premix burner. In FLOX, λ is calculated once for the worst-case condition and held constant , no dynamic re-tuning, because there is no flame stability criterion.

Dual-mode operation. One advantage of the DTO. The propane flame continues to burn uninterrupted as pyrolysis gases enter through a secondary port, no transition in operating mode is required. FLOX needs a deliberate switch once the chamber reaches 850 °C. For OACTIV-27 this transition is less problematic because of the pyrolysis ramp-up phase that is already needed to heat the kiln, so no additional warm-up time is added. But it does require a two-circuit air system and an interlock on chamber temperature, which a DTO does not require.

Chosen equipment for Case 1. The DTO cannot guarantee complete PAH destruction in the cooler peripheral zones. FLOX can, and the industrial data confirm it [17]. That is why FLOX is retained despite the simpler dual-mode operation of the DTO.

Case 2: COSTAIR,PMB, DTO and FLOX.

Two further architectures: COSTAIR [31] and the porous media burner (PMB) [32] were designed for a more specific case. Both were developed for low calorific value (LCV) gases: COSTAIR was tested on biomass gasification gas, mine gas, landfill gas and wood gas, all conditioned streams with negligible tar content [31]. The PMB was similarly validated on landfill gas and light pyrolysis off-gas fractions, and cannot tolerate condensable tars at all: any tar deposition in the ceramic matrix pores would cause fouling and require disassembly for cleaning [32].

Neither architecture was designed or validated for the raw, tar-laden volatile stream of a slow pyrolysis batch cycle. They therefore apply only to Case 2 if we condense all the heavy tars. For Case 1 (all gases burned in vapour phase), only the DTO and FLOX are viable candidates, and the choice between them has been made based on the emissions and stability arguments established above.

Comparison between COSTAIR and PMB. Beyond the shared limitation to clean LCV gases, the two architectures differ in operating principle, robustness and maintenance profile.

Operating principle. COSTAIR retains a distributed flame: air is injected progressively along the combustion axis so that no cross-section ever sees a stoichiometric temperature peak, but combustion still occurs through a classical flame mechanism [31]. The PMB has no flame at all: the unburned premixed gas-air stream is pre-heated by conduction through the ceramic matrix before reaching the reaction zone, producing a superadiabatic oxidation that extends the stability envelope below the conventional Lower Flammability Limit [32].

Robustness and maintenance. COSTAIR uses conventional metallic and refractory components: it tolerates thermal shock during cold-start batch cycles and can be inspected and maintained without disassembly. The PMB ceramic matrix (SiC or Al_2O_3) is fragile under thermal cycling and must be removed and inspected if fouled by tar condensation [32]. A batch kiln that cold-starts every five-hour cycle is a difficult environment for ceramics.

Conclusion of the comparison. Between the two, COSTAIR is the more practical option: it is industrially validated at the right power scale, robust to thermal cycling, and tolerant of the moderate tar content that may remain in the vapour stream after condensation of the heavy PAH fraction. But if we compare it to the FLOX and DTO, the DTO technology in this case is the retained one. The main difference between case 1 and 2 is the removal of the Heavy tars, and the decision made for case 1 was motivated by the guaranteed destruction of PAH by the FLOX burner. In this case the most refractory PAHs are condensed and will not pose a problem for the burner therefore the DTO burner who is easier to operate is chosen.

4.3 Stoichiometry and propane sizing.

The stoichiometric air demand is computed in two independent steps.

Step 1 , General combustion equation. For any combustible species of formula $C_xH_yO_z$, the stoichiometric O_2 coefficient follows from the oxygen balance:

$$n_{O_2} = x + \frac{y}{4} - \frac{z}{2} \tag{27}$$

The complete combustion equation with excess air ratio λ is:

$$\begin{aligned} C_xH_yO_z + \lambda\, n_{O_2}(O_2 + 3.76\,N_2) \;\rightarrow\; & \\ x\,CO_2 + \frac{y}{2}\,H_2O + 3.76\,\lambda\, n_{O_2}\,N_2 & \\ + (\lambda - 1)\, n_{O_2}(O_2 + 3.76\,N_2) & \end{aligned} \tag{28}$$

The last term is the non-reacted excess air leaving with the flue gas. At $\lambda = 1$ it vanishes; for $\lambda > 1$, a fraction $(\lambda - 1)/\lambda$ of the supplied air does not react.

Among the tar species produced during slow pyrolysis, the most thermally refractory species require the highest n_{O_2} and the highest temperature for complete oxidation [23, 24]. This value of n_{O_2} sets a *minimum* on the O_2 that must remain available at the end of the residence time: since CO, H_2 and CH_4 react faster [23], they consume their share of O_2 first, leaving the heavier tars to react last against the residual O_2 concentration. If $\lambda = 1$, that residual tends to zero and destruction of the most refractory species stops before completion regardless of temperature or residence time. The excess air ratio $\lambda > 1$ is therefore not optional.

The stoichiometric air volume (per Nm^3 of pyrolysis gas) is the sum of Eq. (27) over all combustible species weighted by their volumetric fractions w_i:

$$V_{\text{air,st}} = \frac{1}{0.21} \sum_i \left(x_i + \frac{y_i}{4} - \frac{z_i}{2} \right) w_i \tag{29}$$

where the sum covers all combustible species in the pyrolysis stream (w_i is the volumetric concentration of each species). The species flow rates $\dot{m}_i(t)$ from SPY allow Eq. (29) to be evaluated at each time step over the batch cycle.

Step 2 , Excess air ratio. Supplying exactly $V_{\text{air,st}}$ ($\lambda = 1$) drives the residual O_2 to zero at the end of the residence time, stopping the oxidation of the most refractory tar species before completion. Experimental data from [30] show that $\lambda \geq 1.3$ is required at 950 °C for complete tar destruction; an upper bound of $\lambda = 1.6$ accounts for local mixing inhomogeneity within the FLOX chamber [27]:

$$V_{\text{air}} = \lambda\, V_{\text{air,st}} \qquad \lambda \in [1.3,\ 1.6] \tag{30}$$

Remark on excess air control. In a conventional burner, the excess air ratio must be adjusted continuously throughout the batch cycle to compensate for the changing LHV and composition of the pyrolysis gas stream; without such adjustment, the flame either blows out when the gas is too lean or risks flashback when it is too rich [28]. In any high-temperature combustion chamber operating above 950 °C, this constraint disappears: any combustible species entering the volume oxidises spontaneously regardless of its instantaneous flow rate or composition, provided the chamber temperature is maintained [29, 30]. The excess air ratio λ must still be calculated for the worst-case condition (peak volatile flow rate, maximum tar content) and held constant thereafter. The lambda probe monitors the residual O_2 to confirm that this setpoint is maintained, but the air supply valve requires no continuous re-tuning.

Link to instrumentation (Annex C). From Eq. (28), the dry mole fraction of residual O_2 in the flue gas produced by burning the full pyrolysis gas mixture at excess air ratio λ is:

$$w_{O_2,\text{dry}} = \frac{0.21\,(\lambda - 1)\, V_{\text{air,st}}}{\sum_i x_i\, w_i + V_{\text{air,st}}\,(\lambda - 0.21)} \tag{31}$$

where $\sum_i x_i w_i$ is the total CO_2 in the dry flue gas (combustion products plus CO_2 already present in the pyrolysis stream), and $V_{\text{air,st}}$ is evaluated from Eq. (29) using the species composition provided by SPY. The numerical value of $w_{O_2,\text{dry}}$ at $\lambda = 1.5$ has been calculated and is presented in a graph in Annex A. This quantity is measured by a zirconia (ZrO_2) oxygen probe placed in the post-chamber duct where the flue gas has cooled below 800 °C. The probe output closes the air-supply control loop: a deviation from the $\lambda = 1.5$ setpoint drives the variable-frequency fan to correct the air flow.

Propane pilot sizing. The minimum propane flow to maintain the FLOX chamber above the auto-ignition threshold follows from the instantaneous energy balance:

$$\dot{m}_{C_3H_8}\,\text{LHV}_{C_3H_8} \;\geq\; \dot{Q}_{\text{loss,chamber}} - \sum_i \dot{m}_i\,\text{LHV}_i \quad (32)$$

where $\sum_i \dot{m}_i\,\text{LHV}_i = \dot{Q}_{\text{pyrogas}}(t)$ is the instantaneous thermal power of the volatile stream predicted by SPY. Design targets: $T \geq 950\,°\text{C}$, residence time $\geq 1\,\text{s}$, $\lambda = 1.5$ [23, 30].

4.4 Additional Equipment.

The additional piece of equipment that needs to be introduced in the Case 2 scenario is the condensation unit. At pilot scale, the simplest implementation is a cylindrical pot with internal metal-mesh identical in principle to the wood-vinegar reservoir of the Biolyser platform, through which the hot volatile stream passes and loses its heavy PAH fraction by condensation on the cooled walls. The liquid drains to a sump with a ball valve for periodic collection; what exits the top is a cleaned vapour stream carrying the lighter oxygenated tars and all non-condensable gases.

Table 3: Design parameters for the two afterburner scenarios.

Parameter	**Case 1**	**Case 2**
Transfer line T (°C)	250–300	150–200
Critical tar group	Class 4–5 PAH	Primary oxygenated
Excess air λ (–)	1.3–1.6	1.2–1.3
Burner type	FLOX	DTO
Chamber T (°C)	950–1050	850
Residence time τ (s)	$\geq$1	$\geq$2
PAH liquid waste	None	Requires disposal
LHV recovered	Full	Partial

Table 3 summarises the two configurations.

5 Conclusions

The choice for the lab prototype is Case 1.

The prototype runs a single kiln, not the two parallel furnaces of the final configuration. In this context, testing if all the pyrolysis gases can be recovered is one of the main questions that the prototype should answer. Case 1 in this context is a better option because it does not waste the main thermal resource of the process and because EU IED 2010/75/EU requires thermal treatment of all process gas streams. Case 1 recovers the full LHV of every volatile fraction; Case 2 condenses and discards part of it.

The consequence of Case 1 is that the transfer lines must be held above 250–300 °C. For the prototype this can be done without external heating: the hot flue gases leaving the FLOX chamber, before being vented, pass through a heat exchanger that wraps the pyrolysis gas transfer lines. The combustion products flow along the outside of the transfer line and the pyrolysis gases along the inside, so that the waste heat from the burner keeps the lines above the tar dew point at no additional energy cost with a counter-flow installation.

The FLOX burner is retained over a conventional design for the reason established in the discussion: once the chamber reaches 850 °C during the propane ramp-up, the transition to flameless mode is automatic, and from that point combustion stability is insensitive to gas composition.

Experimental validation. Three modelling assumptions will be tested on the prototype: the particle-to-batch extrapolation (A1), the macroparticle Biot regime (A2), and the one-way SPY-to-reactor coupling (A4). Thermocouple measurements at the centre and surface of the biomass bed provide the primary check on A1 and A2; a comparison between the predicted $\dot{Q}_{burn}$ trajectory and the logged propane consumption will validate the energy balance and, by extension, A4.

Acknowledgements

This work was supported by the OACTIV-27 project partnership between UCLouvain, CRA-W (Walloon Agricultural Research Centre), and Fours H&C. I would personally like to thank Nicolas Parmentier who helped me throughout the year and answered every question that I had, he has given me lots of resources to inform myself about the subject and gave me access to SPY. I am also grateful to have a great supervisor such as Professor Hervé Jeanmart who helped me a great deal in the writing of this article.
Finally I would like to thank my parents, sister, girlfriend and friends who supported me throughout all the hard periods during my studies.

A $V_{air,st}$ plot

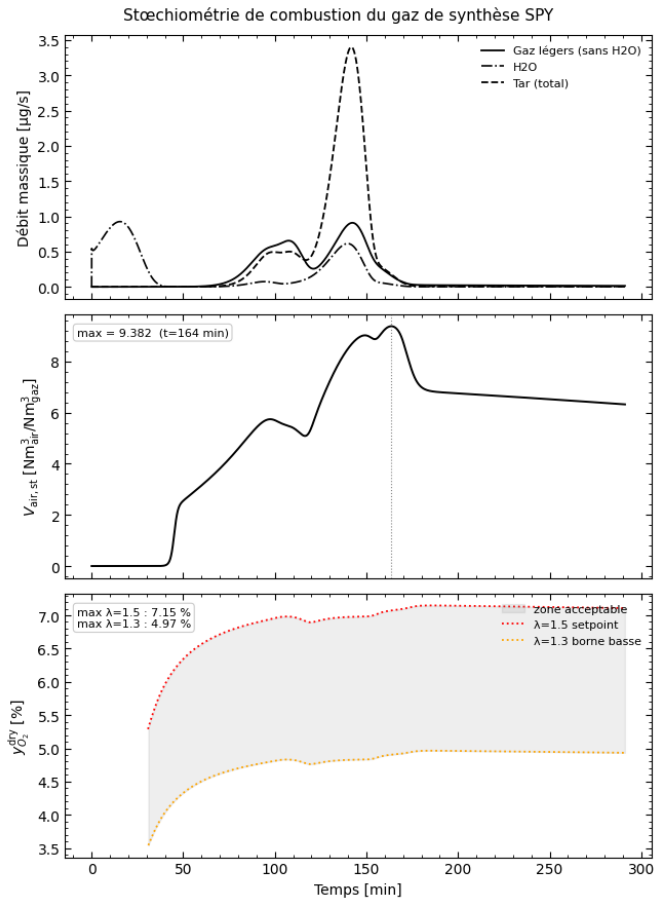

Figure 11:

B SPY details

B.1 Thermal and Mass Transport in the Porous Matrix

In a fibrous wood particle, heat and mass transport are anisotropic. Both the thermal conductivity and the permeability are higher along the fibres (z direction) than across them (r direction), and Blondeau's choice of physical parameters reflects this anisotropy.

The intrinsic thermal conductivities are taken from the correlations of Thunman et al., as adopted in [7]: $k_{b,\parallel} = 0.73$ W m^{-1} K^{-1} and $k_{b,\perp} = 0.52$ W m^{-1} K^{-1} for biomass, and $k_c = 1.47 + 0.0011\,T$ W m^{-1} K^{-1} for char, treated as isotropic. The gas-phase conductivity is constant, $k_g = 0.0258$ W m^{-1} K^{-1}. The effective directional conductivities $k_{eq,r}$ and $k_{eq,z}$ are weighted averages of the solid and gaseous contributions and include an equivalent radiative term that accounts for radiation across the pores [7]. For typical apparent densities between 300 and 800 kg m^{-3}, this yields $k_{eq,\parallel}$ in the range 0.2–0.4 W m^{-1} K^{-1} and $k_{eq,\perp}$ between 0.1 and 0.2 W m^{-1} K^{-1}, in line with the constant-conductivity values used in simplified models [7].

The intrinsic densities of biomass and char are $\hat{\rho}_b = 1500$ kg m^{-3} and $\hat{\rho}_c = 2000$ kg m^{-3} [7], and the porosity is deduced from the apparent densities through $\varepsilon = 1 - \rho_b/\hat{\rho}_b - \rho_c/\hat{\rho}_c$. As pyrolysis proceeds, the apparent density falls from approximately 650 kg m^{-3} for fresh beech to roughly 200 kg m^{-3} for the resulting char, and ε rises accordingly.

The permeabilities follow the values [7] adopts from the previous literature: $B_{r,b} = 10^{-14}$ m^2 and $B_{z,b} = 10^{-12}$ m^2 for biomass, with two orders of magnitude of anisotropy, and $B_{r,c} = B_{z,c} = 10^{-11}$ m^2 for char, taken as isotropic. The gas viscosity is a single constant for all species, $\mu = 3 \times 10^{-5}$ kg m^{-1} s^{-1}. Local effective values are interpolated as a function of the conversion degree.

Species diffusion is described with effective binary diffusion coefficients in the range 10^{-6}–10^{-3} m^2 s^{-1} depending on species class (gas, tar, inert), as in [7]. Sensitivity analyses reported in the same work show that the diffusion coefficient has only a marginal effect on the global mass loss curve, so a precise value is not critical for the energy balance application targeted here.

B.2 Shrinkage

The solid matrix contracts as decomposition proceeds. SPY treats this anisotropically: radial and longitudinal shrinking factors s_r and s_z scale linearly with the local conversion degree and the mesh deforms via a moving-grid algorithm that keeps the orthogonality of the discretisation [7]. The default final shrinking factors are $s_{r,\mathrm{fin}} = 0.6$ and $s_{z,\mathrm{fin}} = 0.75$, corresponding to 40 % radial and 25 % longitudinal contraction at full pyrolysis, in agreement with the values reported by Bellais and used in [7]. For a 15 mm initial radius, the final radius is approximately 12 mm.

Shrinkage has two competing effects on conversion time, both discussed in [7]: it reduces the surface area exposed to

convection, which slows external heating, and it shortens the conduction path between surface and centre, which accelerates internal heating. The net outcome depends on the Biot number and is not monotonic.

B.3 Governing Equations

SPY solves four coupled partial differential equations [7]. Energy conservation is written

$$(\rho c)_{tot}\frac{\partial T}{\partial t} = \nabla\cdot(k_{eq}\nabla T) - \rho_g c_{p,g}\mathbf{u}\cdot\nabla T + \omega_h \qquad (33)$$

where $(\rho c)_{tot} = (1-\varepsilon)(\rho c)_s + \varepsilon\sum_i \rho_i c_{p,i}$ is the volumetric heat capacity of the porous medium, $\mathbf{u}$ the mass-averaged gas velocity and ω_h the chemical heat source. As shown in [7], ω_h contains the heats of reaction at a reference temperature plus a sensible-heat correction that accounts for the difference between species heat capacities, so that the formulation is consistent with first-principles enthalpy balance even when the reaction temperature differs from the reference state.

Solid species mass conservation reduces to a local source term, since the solid is immobile:

$$\frac{\partial \rho_{s,j}}{\partial t} = \omega_{s,j} \qquad (34)$$

Gaseous species mass conservation includes diffusion and convection:

$$\varepsilon\frac{\partial(\rho_g Y_{g,i})}{\partial t} = \nabla\cdot(\rho_g D_{eff,i}\nabla Y_{g,i}) - \nabla\cdot(\rho_g Y_{g,i}\mathbf{u}) + \omega_{g,i} \qquad (35)$$

Momentum conservation is not solved explicitly: SPY assumes that the gas flow inside the pores is creeping and follows Darcy's law,

$$\mathbf{u} = -\frac{B}{\mu}\nabla p \qquad (36)$$

where B is the directional permeability tensor. Pressure is recovered from a Poisson-like equation derived from total mass conservation [7].

B.4 CRECK 2020-03 Kinetic Mechanism

The chemical source terms $\omega_{s,j}$ and $\omega_{g,i}$ are evaluated from the CRECK 2020-03 mechanism [11], which is the current evolution of the multi-step competitive scheme originally proposed by Ranzi and co-workers and used in [7]. CRECK 2020-03 retains the structure of two-step decomposition for each primary constituent: an endothermic activation step producing an active intermediate (CELLA, HCEA, LIGA) followed by competitive parallel channels yielding char, tar and gas in temperature-dependent proportions. Slow heating shifts the branching towards char and water, fast heating towards levoglucosan and lighter volatiles [11]. All reaction rates follow Arrhenius form, $k = A\exp(-E/RT)$, with the kinetic constants and reaction enthalpies tabulated in the CRECK release notes. Thermodynamic data (formation enthalpies, heat capacities) are obtained from the CRECK database via Cantera and are evaluated at 700 K, the reference temperature consistent with the pyrolysis range explored here.

B.5 Configuration and Boundary Conditions

The boundary conditions on the temperature field combine convection and radiation [7]:

$$k_{eq,r}\left.\frac{\partial T}{\partial r}\right|_{r=L_r} = h_{eq}(T_e - T) + \varepsilon_w\sigma(T_{rad}^4 - T^4) \qquad (37)$$

with an analogous expression on the axial boundary. T_e is the temperature of the surrounding gas, T_{rad} that of the radiating surface and ε_w the emissivity of the particle surface.

For the OACTIV-27 reference simulation, the operating conditions are: external heat transfer coefficient $h_{ext} \approx 30$ W m^{-2} K^{-1} representative of forced convection in the flue-gas annulus; gas temperature $T_e(t)$ prescribed as a linear ramp from 20 °C to 400 °C at 2.2 °C min^{-1} followed by a 120 min plateau at 400 °C; ambient pressure $p = 101325$ Pa; inert atmosphere (no oxidiser); uniform initial temperature $T_0 = 20$ °C. The particle surface is taken as grey with $\varepsilon_w = 0.9$.

C instrumentation

The instrumentation architecture differs between the two operating modes of the FLOX chamber.

During the ramp-up phase, the burner operates in conventional flame mode (air supply 2 active, per the dual-mode design of [29]). Chamber temperature is tracked by two type-N nicrosil–nisil thermocouples (IEC 60584-1, continuous service to 1300 °C), preferred over type-K for this application because type-K exhibits significant positive drift in long-term oxidising service above 1100 °C [33]. A UV photocell flame detector (∼310 nm, per EN 746-2 §5.5) monitors the propane pilot continuously during this phase; loss of signal triggers immediate closure of the pyrolysis-gas admission valve and activates a safety interlock before the pilot can be re-established.

Once the chamber reaches the FLOX transition temperature (∼850 °C), air supply 2 is closed and supply 3 is activated. In this mode, the UV flame detector is intentionally bypassed: the absence of a UV signal is the expected normal condition in flameless operation, not a fault. Safety monitoring shifts to a temperature-based interlock , if the chamber temperature measured by either thermocouple drops below 850 °C, the fuel supply is cut automatically, since flameless oxidation cannot be sustained below the auto-ignition threshold [29]. This replaces the flame-signal interlock used during ramp-up.

Excess air is controlled in closed loop throughout both phases by a wide-band zirconia (ZrO_2) lambda probe in the post-chamber duct ($T_{90} < 4$ s, range 0.1–25 % O_2). During flame mode the setpoint is tuned for flame stability; during FLOX mode it is held at $\lambda \approx 1.5$ (∼8 % O_2 dry), the value required to sustain complete naphthalene destruction [30]. Air supply 3 (the FLOX nozzle ring) carries a single thermal mass-flow meter (IEC 61508 SIL-1 capable); a variable-frequency fan translates the lambda signal into corrected nozzle air flow. Propane is metered

by a Coriolis controller during ramp-up and maintained at minimum pilot flow during FLOX steady-state. A capacitive pressure transmitter on the chamber maintains a slight negative pressure (-0.5 to -2 mbar) to prevent leakage of unburned pyrolysis gas into the surrounding structure [34].

D Detailed descriptions

D.1 FLOX: Operating principle and stability criteria.

A conventional flame requires a local balance between the flow velocity and the laminar flame speed; this balance depends on species concentrations, flow velocity, temperature, pressure, and geometry [29]. A useful way to quantify the dilution of fresh reactants by recirculated exhaust gas is the recirculation rate $K_v = \dot{m}_{\text{exhaust}}/\dot{m}_{\text{air}}$. Flammability limits for hydrocarbon–air mixtures show that a stable flame can only be sustained for $K_v < 0.5$: below this threshold the mixture is still within the flammable envelope [29]. Above it, the fresh reactants are so diluted by inert combustion products that no flame front can form. Flameless oxidation exploits precisely this regime: by designing the geometry so that the air jets entrain a large volume of recirculated exhaust before contacting the fuel, the system operates permanently at $K_v \gg 0.5$, making a discrete flame structurally impossible [29]. In this chamber, pyrolysis gases enter as the fuel stream at step II and are not to be confused with the recirculated exhaust gas of step I, which consists of the combustion products (CO_2, H_2O, N_2) already formed within the chamber itself.
Process steps and burner design. [29] describe the FLOX process in three idealised steps. In step I, combustion air mixes with recirculated exhaust gas; in step II, fuel is added to this already-diluted air stream. Because the mixture entering step II is heavily inerted by exhaust, the adiabatic temperature rise is only a few hundred Kelvin regardless of fuel composition, and the simplifying assumption "mixed is burnt" applies [29]. Step III withdraws the released energy from the combustion products and maintains the chamber at the temperature level required for step II to self-sustain. The technical realisation uses two independent air supplies (Fig. 11 of [29]).

During start-up, air supply 2 and fuel nozzle 4 feed a central primary combustion chamber 5: the burner operates as a conventional high-velocity torch with spark ignition and a stabilised flame, heating the kiln in the normal fashion. Once the chamber reaches the set-point temperature, air valve 2 is closed and supply 3 is activated; air now enters through nozzles 6 arranged concentrically around chamber 5. The resulting air jet A entrains both exhaust gas and fuel jet B before they meet in reaction zone C, where the combustion products have already diluted both streams to $K_v \gg 0.5$. The recirculation rate is set by the geometry of the nozzle arrangement and requires no active control [29].

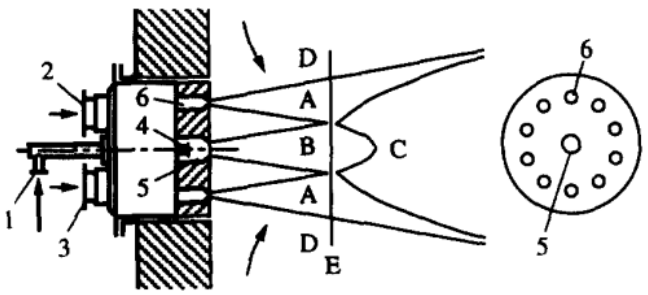

Figure 12: Fig. 11 of [29]: Burner for flame and flameless oxidation mode.

Pre-heating and applicability to OACTIV-27. Maintaining the mixture temperature above the auto-ignition threshold throughout step II is the only precondition for flameless operation. [29] note that air preheat can help meet this condition but is not compulsory [29]. In the OACTIV-27 context, the condition is met automatically: the propane ramp-up phase that is already required to drive the biomass to pyrolysis temperature also serves as the FLOX warm-up phase. By the time pyrolysis gases begin to emerge, the chamber walls are at 850–950 °C. The dual-mode burner (flame during ramp-up, flameless during steady-state) is therefore a good technology to use.

Temperature levels, tar destruction, and emissions. Measurements reported by [29] in sealed furnace tests show that flameless operation sustains bulk chamber temperatures in the range 1000–1200 °C, well above the 1100 K threshold required for the complete oxidation of naphthalene, the most refractory tar species [23, 29]. Crucially, temperature uniformity is a defining feature of the FLOX regime: the absence of a localised flame front suppresses thermal gradients and eliminates hot spots. [29] further establish that thermal NOx formation is reduced by one to two orders of magnitude compared with conventional high-velocity burners, because NOx production is exponentially sensitive to peak temperature rather than mean temperature [29]. Industrial validation on PYREG-class units confirms CO below 100 mg Nm^{-3} and greater than 99 % PAH destruction [17], consistent with the NOx values below 6 ppm reported by [27] for low-calorific-value gases in a FLOX micro-turbine combustor [27].

Conclusions from [29]. The authors conclude that flameless oxidation is achievable whenever the mixture temperature throughout the combustion space exceeds the auto-ignition temperature of the fuel. The process is insensitive to fuel composition and LHV fluctuations, since ignition depends on temperature rather than on a flame-speed balance. This is one of the main reasons to choose this technology, because the syngas composition is variable during the whole process of the pyrolysis. Otherwise we would have to do a continuous re-tuning of the air supply to avoid either flame blow-out or flashback [28]

D.2 Direct-fired thermal oxidiser , retort system (CBFE, [12])

The most directly applicable reference for the OACTIV-27 prototype is the retort pyrolysis unit developed at *Charbon de bois feuille d'érable Inc.* (CBFE, Ste-Christine

d'Auvergne, Québec) as part of an industrial PhD project at UQTR [12]. The system was designed specifically for slow pyrolysis of hardwood , sugar maple (*Acer saccharum*), yellow birch (*Betula alleghaniensis*) and beech (*Fagus grandifolia*) , with full recovery of the pyrolysis gas stream. Its operating principle maps closely onto the OACTIV-27 constraints: indirect heating of a sealed biomass charge, with all pyrolysis gases directed to a combustion chamber that substitutes for propane once devolatilisation begins.

System architecture. The unit comprises five interconnected components.

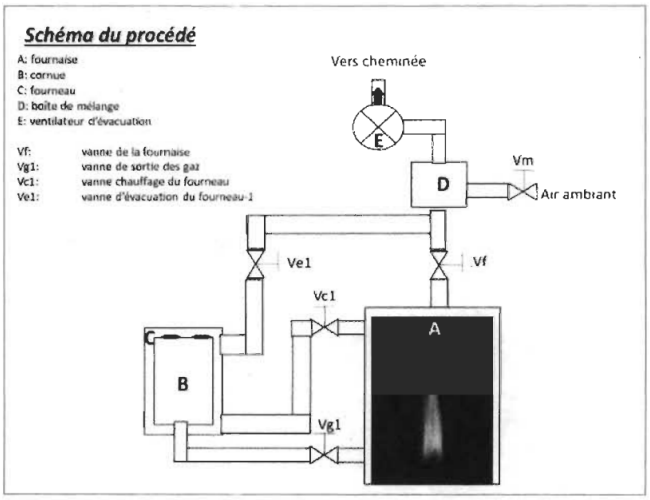

Figure 13: Fig. 3.3 of [12]: schematic of the process of pyrolysis at CBFE

A , Combustion chamber (fournaise). A propane-fired direct thermal oxidiser operating continuously at 1500 °F (815 °C). It serves two simultaneous functions: it is the primary heat source that drives the indirect heating of the retorts, and it is the afterburner that incinerates all pyrolysis gases at 815 °C for more than one second [12]. The propane pilot remains lit throughout the cycle; its flow is reduced to the minimum required to hold the setpoint when pyrolysis gas from the retorts provides sufficient energy.

B , Steel retort (cornue). A sealed steel vessel of 0.17–0.19 m^3 internal volume, designed to hold approximately 60 kg of biomass. The lid is sealed with a ceramic fibre gasket cord (Kwool) to ensure air tightness and prevent any contact between the biomass and ambient oxygen throughout the cycle. A drain valve V_{e1} at the base of the retort evacuates pyrolysis gases and condensed liquid (pyrolytic liquid) towards the combustion chamber. The biomass therefore carbonises in a fully inert atmosphere at all times [12].

C , Insulated furnace shell (fourneau). A steel shell dimensioned to fit the retort exactly, leaving a narrow annular gap through which hot combustion gases from the chamber circulate around the retort exterior. Admission of these gases is controlled by valve V_{c1}. The shell lid is seated in a ceramic fibre ring to seal the top of the annular space. A port at the base of the shell allows pyrolysis gases to transit from the retort drain to the combustion chamber. Four such shells are connected in parallel to a single combustion chamber, which allows two retorts to be in active pyrolysis while two others are in the pre-heating phase, maximising the recovery of thermal energy from the chamber exhaust and reducing propane consumption [12].

D , Mixing box. A steel plenum downstream of the furnace shells that dilutes the hot combustion exhaust or furnace outlet gas with ambient air. A motorised butterfly damper V_m and a closed-loop temperature controller regulate the mixing ratio to hold the outlet temperature at approximately 300 °F (150 °C) before the exhaust fan and chimney. This prevents thermal damage to the fan and maintains safe conditions in the exhaust ductwork [12].

E , Exhaust fan. An induced-draft centrifugal fan draws gases from the mixing box outlet and pushes them to the chimney. By maintaining a slight negative pressure throughout the circuit, the fan ensures that pyrolysis gases are continuously aspirated out of the retort through V_{e1} during the active pyrolysis phase, preventing pressure build-up inside the sealed vessel [12].

Valve positions and operating sequence. The cycle begins with the combustion chamber burning propane at 815 °C. In the initial standby state, V_{g1} (pyrolysis gas admission to chamber) is closed, V_f (combustion chamber exhaust to mixing box) is open, and V_{c1}, V_{e1} are closed. To begin heating a loaded retort, the valves are switched: V_{g1} remains closed, V_{c1} opens (admitting chamber hot gases to the furnace shell), V_{e1} opens (connecting retort drain to chimney circuit), and V_f closes (redirecting chamber exhaust through the furnace shell rather than directly to the mixing box). Hot gases at approximately 700 °F (370 °C) at the furnace inlet now circulate around the retort, heating the biomass charge indirectly [12].

Once the endothermic drying phase is complete, the devolatilisation reaction starts and pyrolysis gases begin to flow. At this point V_{g1} is opened: pyrolysis gases are aspirated directly into the combustion chamber and incinerated at 815 °C for $\tau > 1$ s. When the biomass temperature reaches approximately 500 °F (260 °C), the exothermic pyrolysis reaction becomes self-sustaining and the biomass no longer requires external heat input. Valves V_{c1} and V_{e1} are closed and V_f is reopened: the furnace shell is disconnected from the circuit and the chamber exhaust returns to the mixing box directly. The propane supply drops to the minimum required to maintain 815 °C, with the pyrolysis gas stream covering the balance of the thermal demand [12].

The internal temperature of the retort can rise to ∼1000 °F (∼540 °C) depending on the degree of conversion targeted. When gas and condensate production at V_{e1} drops to zero, pyrolysis is considered complete. Valve V_{g1} is closed, and the retort is extracted from the furnace shell. Its base is immediately immersed in a sand box that seals the drain port and prevents air from entering the hot charcoal during the 48-hour passive cooling period, which avoids re-combustion of the product [12].

A complete cycle from loading to extraction lasts approximately five hours. Each retort yields approximately 45 lbs (∼20 kg) of charcoal at a mass yield of 30–35 % on a dry basis , roughly double the 17 % achieved in the traditional casemate kilns also operated by CBFE, where

part of the wood charge is consumed as fuel to heat the rest [12]. This higher yield is the direct consequence of indirect heating: no biomass is burnt to drive the process. Economically, the system is not viable above 35 % initial moisture content in the biomass, as the endothermic drying phase becomes too long relative to the productive pyrolysis phase [12].

Combustion chamber type. The afterburner is a direct-fired thermal oxidiser: pyrolysis gases enter a refractory-lined chamber where a propane pilot sustains the temperature and provides a permanent ignition source, with no forced aerodynamic recirculation.

Adaptation to OACTIV-27. The retort architecture maps directly onto the OACTIV-27 concept: a sealed biomass vessel inside a heated shell, with all pyrolysis gases directed to a combustion chamber operating on propane backup. The valve logic, the four-in-parallel furnace shell arrangement, and the sand-box cooling can all be adapted without conceptual modification. The single upgrade is the combustion chamber: from a DTO at 815 °C to a FLOX chamber at 950–1100 °C. This raises the operating temperature above the IED threshold, ensures complete destruction of aromatic tar species in all zones of the chamber, eliminates the need for continuous propane during peak devolatilisation, and reduces NOx by one to two orders of magnitude.

D.3 Continuous air staging

The COSTAIR (Continuous Air Staging) concept was developed at Gaswärme-Institut e.V. Essen (GWI) within the nine-partner EU Bio-Pro project on new burner technologies for low-grade biofuels [31]. FLOX was developed in parallel within the same project by a different partner; COSTAIR was the approach taken specifically by GWI. Both were conceived to address the same fundamental problem: conventional burner geometries do not guarantee sufficient flame stability for LCV gases, and the resulting high CO and NOx emissions make them environmentally unacceptable for batch pyrolysis applications [31].

Operating principle and burner geometry. The COSTAIR burner is built on a coaxial tube geometry.

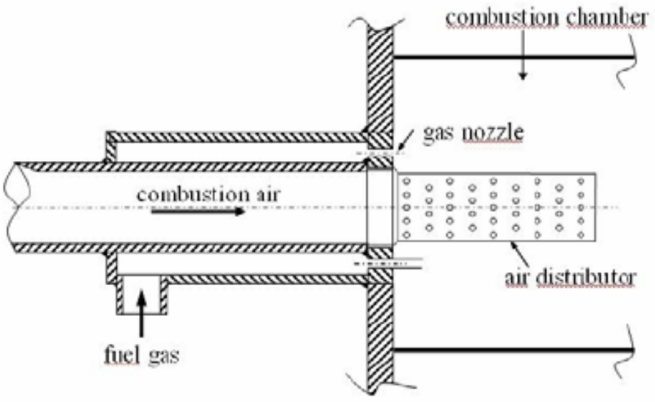

Figure 14: Fig. 1 of [31]: sketch of the COSTAIR burner.

Combustion air flows through the inner tube; fuel flows through the surrounding outer annular ring. The inner tube does not terminate at a single nozzle as in a conventional burner. Instead, it ends in an *air distributor* , a hollow body fitted with a large number of small openings distributed evenly along its contour. Air exits progressively through these openings as the flow advances through the combustion zone, distributing the oxidiser continuously along the combustion axis rather than injecting it all at the inlet. Fuel is injected through multiple holes arranged in one or more rows around the air distributor perimeter, with adjustable jet direction. Both the air and fuel streams can be given a swirl component by an appropriate angle of the injection holes, which promotes mixing and further stabilises combustion [31].

The consequence of this geometry is that no single cross-section of the combustion chamber ever sees a stoichiometric or near-stoichiometric fuel-air mixture at the peak adiabatic temperature. Air is added gradually as the partially burned mixture travels downstream: the local equivalence ratio at any axial position is therefore lower than the overall mixture ratio, and the peak temperature is suppressed throughout the chamber length. Every parcel of fuel nonetheless eventually encounters sufficient oxygen for complete burnout, because the distributed injection guarantees coverage over the full chamber volume [31].

Test conditions and gas compositions. All experiments were conducted at atmospheric pressure ($p \approx p_{\mathrm{atm}}$), with combustion air at ambient temperature ($T_{\mathrm{air}} \approx 20\,^{\circ}\mathrm{C}$) and fuel preheated to 400 °C through two electrically driven pre-heaters [31]. We list the five gas mixtures tested, covering the range of LCV sources of industrial interest:

- Biomass gasification gas, mixture 1: 5 % CH_4, 20 % H_2, 15 % CO_2, 10 % CO, 50 % N_2; LHV $\approx 5.4\,\mathrm{MJ/Nm^3}$
- Biomass gasification gas, mixture 2: 0 % CH_4, 21 % H_2, 14 % CO_2, 10 % CO, 55 % N_2; LHV $\approx 4.1\,\mathrm{MJ/Nm^3}$
- Mine gas: 25 % CH_4, 10 % CO_2, 65 % N_2; LHV $\approx 9\,\mathrm{MJ/Nm^3}$
- Landfill gas: 20 % CH_4, 80 % N_2; LHV $\approx 7.2\,\mathrm{MJ/Nm^3}$
- Wood gas: 5 % CH_4, 15 % H_2, 15 % CO, 15 % CO_2, 50 % N_2; LHV $\approx 3.6\,\mathrm{MJ/Nm^3}$

Experimental results at 30 kW. Across all five gas mixtures, the COSTAIR burner produced a stable, non-pulsating flame. NOx emissions stayed below 28 ppm and CO between 4 and 8 ppm at 3 vol % O_2 in the flue gas , significantly below the EU Bio-Pro project targets (NOx $<150\,\mathrm{mg/Nm^3}$, CO $<30\,\mathrm{mg/Nm^3}$) [31]. The operating pressures of gas and air before the combustion chamber were very low for all gas mixtures, indicating low pressure-drop losses in the distributor geometry.

The wall temperature distribution along the combustion chamber, measured at multiple axial positions, revealed a characteristic behaviour that depends on the H_2 content of the gas. For biomass gasification gas (mixture 1, ∼20 vol %

H_2), the high laminar flame speed of hydrogen-rich mixtures produces a compact, short flame concentrated immediately around the air distributor: wall temperatures are high near the distributor and decrease steadily downstream. For landfill gas (no H_2), the lower burning velocity produces a longer, more distributed flame: wall temperatures are lower near the distributor and significantly higher further downstream. This composition-dependent flame length is a structural feature of COSTAIR that must be accounted for in the chamber design for a batch pyrolysis application where the H_2 fraction shifts over the cycle [31].

Scale-up to 200 kW. The 200 kW burner was tested on biomass gasification mixture 2 (LHV $\approx 4.1\,\mathrm{MJ/Nm^3}$) at the same operating conditions as the 30 kW unit. The combustion behaviour was identical to the small-scale results, confirming the validity of the scale-up methodology and establishing COSTAIR as a technology with demonstrated industrial relevance at power levels directly comparable to the OACTIV-27 requirement (∼30 kW continuous) [31].

Comparison with FLOX and suitability for OACTIV-27. COSTAIR and FLOX share the same parent project and the same fundamental goal. FLOX eliminates the flame entirely by operating above the flammability limit ($K_v > 0.5$); COSTAIR retains a distributed flame but prevents hot spots through continuous air staging. FLOX achieves lower NOx (<6 ppm vs. <28 ppm) and is structurally insensitive to the H_2-dependent flame shape noted above, which matters in a batch cycle where gas composition varies continuously. The advantage of COSTAIR over FLOX is that it does not require the chamber to be pre-heated to 850 °C before stable operation, simplifying cold-start. For OACTIV-27, where the pyrolysis gas LHV stays well above $3.6\,\mathrm{MJ/Nm^3}$ at peak devolatilisation and the propane ramp-up naturally provides the FLOX warm-up, neither advantage of COSTAIR outweighs the superior NOx performance and composition insensitivity of FLOX.

D.4 Porous media burner

The porous media burner applied to pyrolysis and landfill gas is documented by Al-Hamamre, Diezinger, Talukdar, von Issendorff and Trimis from TU Bergakademie Freiberg (Germany) [32]. Diezinger's concurrent doctoral work at Universität Erlangen-Nürnberg on multi-fuel porous burners for fuel-cell systems provides complementary details on the same experimental platform. The study is directly application-oriented: the LCG mixtures chosen for testing were specifically representative of landfill and waste pyrolysis off-gas, not generic combustion research gases.

The superadiabatic combustion principle. In a conventional free-flame burner, the maximum temperature achievable is the adiabatic flame temperature , the temperature the products would reach if all the reaction enthalpy were retained in the gas phase with no heat losses. For an LCV gas (high inert content, low H_2), this adiabatic temperature may be only 900–1000 K, insufficient to sustain stable ignition or complete tar oxidation. A porous media burner circumvents this limit through *internal heat recirculation*: the solid ceramic matrix conducts heat from the hot post-flame zone back upstream to the cold unburned mixture [32]. The unburned gas-air mixture therefore arrives at the reaction zone pre-heated , not by an external device, but by the combustion products already in the matrix. The result is a local flame temperature that exceeds the adiabatic flame temperature of the free mixture: hence "superadiabatic". The practical consequence is that mixtures well below the conventional Lower Flammability Limit can sustain stable combustion inside the matrix, provided the imposed flow velocity and thermal load are within the stability envelope [32].

Burner geometry. The standard PMB design used in the Trimis group's work is a two-section cylindrical or rectangular chamber. The *upstream section* (preheating zone) is packed with a finer-pored ceramic material , typically Al_2O_3 beads or a low-porosity foam , whose pore size is smaller than the flame quenching distance for the fuel-air mixture. This prevents the flame from propagating backwards into the unburned gas supply (flashback arrestor). The premixed LCG-air mixture flows through this upstream section and is pre-heated by conduction from the downstream hot zone. The *downstream section* (combustion zone) is packed with a higher-porosity ceramic foam , SiC or Al_2O_3 with larger pore size , where the superadiabatic flame is stabilised. The solid matrix in this zone stores and re-radiates heat, creating the uniform temperature field that suppresses NOx formation and allows operation at equivalence ratios well below unity [32].

Matrix materials and their trade-offs. Al-Hamamre et al. tested both SiC (silicon carbide) and Al_2O_3 (aluminium oxide) structures [32]. The two materials have complementary properties:

SiC has high thermal conductivity, which promotes the upstream heat recirculation that drives the superadiabatic effect, and shows good thermal shock resistance, important for handling transient temperature changes at start-up and shut-down. However, SiC oxidises above approximately 1400 °C and is not chemically stable at the highest temperatures reached in the combustion zone during high-LHV operation.

Al_2O_3 is chemically stable at temperatures above 1600 °C and is therefore preferred for the combustion zone when peak temperatures are high. Its thermal conductivity is lower than SiC, which limits the upstream heat recirculation efficiency, and its poor thermal shock resistance makes it vulnerable to cracking under rapid thermal cycling , a significant concern for batch pyrolysis applications where the burner undergoes a cold start every cycle [32].

Numerical and experimental methodology. The investigation proceeded in two parallel tracks [32]. Numerically, the adiabatic flame temperatures and laminar burning velocities of the LCG test mixtures were computed using GRI Mech. 3.0 with the CHEMKIN software suite. These calculations established the theoretical combustion envelope , the range of mixture compositions and equivalence ratios that can in principle sustain a flame , before any geometry was committed to hardware. A separate 3D numerical code then simulated the full combustion process inside the porous structure, accounting for the coupled gas-phase chemistry, heat conduction in the solid matrix, and radiation heat transfer between the ma-

trix and the gas. This simulation provided temperature and species concentration fields at different thermal loads and inlet temperatures.

Experimentally, the operational range of both SiC and Al_2O_3 burners was mapped at different power rates and educt temperatures. Three parameters were systematically varied: (1) the combustion zone properties , porosity and thermal conductivity of the matrix; (2) the thermal load; and (3) the educt temperature (the temperature of the premixed LCG-air mixture at the burner inlet). All three were found to affect both the stability envelope and the peak superadiabatic temperature. Higher matrix thermal conductivity expands the stability envelope by improving heat recirculation; higher educt temperature reduces the heat recirculation requirement and extends the lean stability limit [32].

Minimum LHV and comparison with other architectures. The combination of superadiabatic heat recirculation and the extended flammability limits of the porous matrix lets the PMB operate on gas streams that would extinguish any free-flame device, with stable combustion reported below 2 MJ/Nm^3 [32], well under the limits of FLOX or COSTAIR. In our case this advantage is not really useful: the pyrolysis gas leaving the kiln at peak devolatilisation sits at 6–10 MJ/Nm^3, far above the FLOX stability threshold. The PMB would only become the better choice if the gas quality dropped below that threshold, and this does not happen in the OACTIV-27 operating window.

Limitations for OACTIV-27. Two practical issues rule out the PMB for this application. The first is thermal shock. The ceramic matrix, whether SiC or Al_2O_3, does not tolerate well the temperature gradients imposed by a propane ramp from ambient to 850 °C, and avoiding cracking requires a controlled warm-up of several hours before each batch [32]. The FLOX chamber does not need this kind of preconditioning. The second issue is fouling. The pores of the upstream preheating section are sized close to the quenching distance, which means even a small amount of tar deposition starts to block them. A single Case 1 cycle, where all gases stay in the vapour phase, may not cause visible damage, but tar accumulates from one cycle to the next and the matrix has to be cleaned or replaced regularly. For a prototype that is meant to be moved between sites and operated outside a laboratory, this maintenance load is not acceptable. The PMB fits much better a continuous-feed process with steady gas composition and a controlled start-up, not a batch kiln running short cycles in the field.

E SPY Simulation Parameters

Table 4: SPY input parameters for cas:e ramp2.2_plat400_120min (beech wood, CRECK 2020-03)

Parameter	Value	Unit
Particle geometry		
Half-radius L_r	15	mm
Half-length L_z	15	mm
Equivalent cylinder	30 × 30	mm
Initial dry density ρ_0 (`wci`)	630	kg/m^3
Intrinsic wood density $\rho_{\mathrm{int,w}}$	1500	kg/m^3
Intrinsic char density $\rho_{\mathrm{int,c}}$	2000	kg/m^3
Radial mesh nodes $n_{r,i}$	30	–
Axial mesh nodes $n_{z,i}$	75	–
Final radial shrinkage $s_{r,\mathrm{fin}}$	0.80	–
Final axial shrinkage $s_{z,\mathrm{fin}}$	0.93	–
Biomass composition (CRECK 2020-03, dry basis)		
Cellulose `CELL` (y_C)	0.4397	–
Hemicellulose soft `HCE-S` ($y_{H,S}$)	0.0000	–
Hemicellulose hard `HCE-H` ($y_{H,H}$)	0.2562	–
Hemicellulose grass `HCE-G` ($y_{H,G}$)	0.0000	–
p-coumaryl lignin `LIGC` ($y_{L,C}$)	0.0583	–
Coniferyl lignin `LIGH` ($y_{L,H}$)	0.0767	–
Sinapyl lignin `LIGO` ($y_{L,O}$)	0.0691	–
Triglycerides `TGL` (y_{TGL})	0.0000	–
Tannins `TAN` (y_{TAN})	0.0000	–
Bound water `BW` (y_{BW})	0.1000	–
Boundary conditions		
Initial temperature T_i	25	°C
Initial/external pressure $p_i = p_e$	10^5	Pa
Wall emissivity ε	0.9	–
Sherwood number Sh_e	0.0	–
Temperature programme (`ramp2.2_plat400_120min`)		
Heating rate	2.2	°C/min
Plateau temperature	400	°C
Ramp duration (20→400°C)	170.8	min
Plateau duration	120	min
Total simulation duration	291	min
Physical properties (gas phase)		
Permeability wood radial $k_{\mathrm{w,r}}$	10^{-14}	m^2
Permeability wood axial $k_{\mathrm{w,z}}$	10^{-12}	m^2
Permeability char $k_{\mathrm{c,r}} = k_{\mathrm{c,z}}$	10^{-11}	m^2
Gas dynamic viscosity μ	3×10^{-5}	Pa·s
Species diffusion coefficient D	5×10^{-5}	m^2/s
Numerical parameters		
Kinetic scheme `flag_kin`	4 (CRECK 2020-03)	–
Time scheme θ_{source}	0.5 (Crank-Nicolson)	–
Minimum time step $\Delta t_{\min}$	0.05	s
Maximum time step $\Delta t_{\max}$	1.0	s
CFL heat/species	0.5	–
STS parameter ν_{heat}	0.001	–
Kinetics ratio r_{kin}	1.0	–
Kinetics threshold $\rho/\rho_{\mathrm{solid}}$	0.1	–
Air mass fraction treatment	complementary	–

References

[1] U.S. Environmental Protection Agency. CompTox chemicals dashboard: PFAS structures in DSSTox (update august 2021). `https://comptox.epa.gov/dashboard/chemical-lists/PFASSTRUCTv4`, 2021.

[2] Agency for Toxic Substances and Disease Registry. Toxicological profile for perfluoroalkyls. Technical report, U.S. Department of Health and Human Services, 2021.

[3] U.S. Environmental Protection Agency. PFAS national primary drinking water regulation. Federal Register, 89 FR 32532, 2024.

[4] U.S. Environmental Protection Agency. Best available technologies and small system compliance technologies for per- and polyfluoroalkyl substances (PFAS) in drinking water. Technical Report EPA 815-R-24-011, U.S. EPA, Washington, DC, 2024.

[5] Mohamed Ateia, Amith Maroli, Nishanth Tharayil, and Tanju Karanfil. The overlooked short-and ultrashort-chain poly-and perfluorinated substances: A review. *Chemosphere*, 220:866–882, 2019.

[6] CRA-W and UCLouvain and Fours H&C. Cahier des charges — oactiv-27 : Sélection et mise au point de biomasses et procédés pour la production de charbons actifs. Internal specification document, Partenariat Oactiv-27, Belgium, 2024.

[7] Julien Blondeau. *Investigation of pulverised biomass combustion: detailed modelling of particle pyrolysis and experimental analysis of ash deposition*. PhD thesis, Ph. D. thesis, Université catholique de Louvain, 2013.

[8] Hervé Jeanmart and Julien Blondeau. Pyrolysis, a key step in the thermochemical conversion of biomass. Lecture series document, Von Karman Institute for Fluid Dynamics, 2020. VKI Lecture Series, UCLouvain/VUB.

[9] Colomba Di Blasi. Modeling chemical and physical processes of wood and biomass pyrolysis. *Progress in energy and combustion science*, 34(1):47–90, 2008.

[10] Karen Koehlert. Activated carbon: Fundamentals and new applications. *Chemical Engineering Progress*, 113(6):32–40, 2017.

[11] P Debiagi, G Gentile, A Cuoci, A Frassoldati, E Ranzi, and T Faravelli. A predictive model of biochar formation and characterization. *Journal of analytical and applied pyrolysis*, 134:326–335, 2018.

[12] Simon Langlois. *Production de charbon activé par recouvrement des gaz de pyrolyse*. PhD thesis, Université du Québec à Trois-Rivières, 2019.

[13] Eliseo Ranzi, Alberto Cuoci, Tiziano Faravelli, Alessio Frassoldati, Gabriele Migliavacca, Sauro Pierucci, and Samuele Sommariva. Chemical kinetics of biomass pyrolysis. *Energy & Fuels*, 22(6):4292–4300, 2008.

[14] Katarzyna Januszewicz, Paweł Kazimierski, Maciej Klein, Dariusz Kardaś, and Justyna Łuczak. Activated carbon produced by pyrolysis of waste wood and straw for potential wastewater adsorption. *Materials*, 13(9):2047, 2020.

[15] Umut Şen, Catarina Nobre, Marta Martins, Margarida Gonçalves, and Helena Pereira. Effect of bark biochars on properties of steam-activated carbons. *Environments*, 11(1):2, 2023.

[16] Calgon Carbon Corporation. Multiple hearth furnace technology for activated carbon production. Technical Bulletin, 2020.

[17] Erlend Sørmo, Ludovica Silvani, Gorm Thune, Helmut Gerber, Hans Peter Schmidt, Andreas Botnen Smebye, and Gerard Cornelissen. Waste timber pyrolysis in a medium-scale unit: Emission budgets and biochar quality. *Science of the total environment*, 718:137335, 2020.

[18] Bio Agri Group. *Biolyser : Manuel d'utilisation*. Bio Agri Group – Renewable Energy, juillet 2024.

[19] Henrik Thunman and Bo Leckner. Thermal conductivity of wood—models for different stages of combustion. *Biomass and Bioenergy*, 23(1):47–54, 2002.

[20] Wendi Guo, C Jim Lim, Xiaotao Bi, Shahab Sokhansanj, and Staffan Melin. Determination of effective thermal conductivity and specific heat capacity of wood pellets. *Fuel*, 103:347–355, 2013.

[21] Sakae Yagi and Daizo Kunii. Studies on effective thermal conductivities in packed beds. *AIChE Journal*, 3(3):373–381, 1957.

[22] Thomas A Milne, Robert J Evans, and Nicolas Abatzaglou. Biomass gasifier"tars": their nature, formation, and conversion. 1998.

[23] Andreas Jess. Mechanisms and kinetics of thermal reactions of aromatic hydrocarbons from pyrolysis of solid fuels. *Fuel*, 75(12):1441–1448, 1996.

[24] Milena Nowakowska, Olivier Herbinet, Anthony Dufour, and Pierre-Alexandre Glaude. Detailed kinetic study of anisole pyrolysis and oxidation to understand tar formation during biomass combustion and gasification. *Combustion and Flame*, 161(6):1474–1488, 2014.

[25] Luc PLM Rabou, Robin WR Zwart, Berend J Vreugdenhil, and Lex Bos. Tar in biomass producer gas, the energy research centre of the netherlands (ecn) experience: an enduring challenge. *Energy & fuels*, 23(12):6189–6198, 2009.

[26] Rita Harb, Rodrigo Rivera-Tinoco, Maroun Nemer, Barbar Zeghondy, and Chakib Bouallou. Towards synthetic fuels production from biomass gasification: Tar content at low temperatures. *Biomass and Bioenergy*, 137:105540, 2020.

[27] Timo Zornek, Thomas Monz, and Manfred Aigner. Performance analysis of the micro gas turbine turbec t100 with a new flox-combustion system for low calorific fuels. *Applied Energy*, 159:276–284, 2015.

[28] Emanuele Graciosa Pereira, Márcio Arêdes Martins, Ralf Pecenka, and Angélica de Cássia O Carneiro. Pyrolysis gases burners: Sustainability for integrated production of charcoal, heat and electricity. *Renewable and Sustainable Energy Reviews*, 75:592–600, 2017.

[29] Joachim A Wünning and Joachim G Wünning. Flameless oxidation to reduce thermal no-formation. *Progress in energy and combustion science*, 23(1):81–94, 1997.

[30] Jesper Ahrenfeldt, Helge Egsgaard, Wolfgang Stelte, Tobias Thomsen, and Ulrik Birk Henriksen. The influence of partial oxidation mechanisms on tar destruction in twostage biomass gasification. *Fuel*, 112:662–680, 2013.

[31] A Al-Halbouni, H Rahms, and Klaus Görner. An efficient combustion concept for low calorific gases. *Renewable Energy and Power Quality Journal*, 1, 03 2007.

[32] Z. AL-Hamamre, S. Diezinger, P. Talukdar, F. Von Issendorff, and D. Trimis. Combustion of low calorific gases from landfills and waste pyrolysis using porous medium burner technology. *Process Safety and Environmental Protection*, 84(4):297–308, 2006. 1st International Conference on Engineering for Waste Treatment.

[33] Thomas Nussbaumer. Combustion and co-combustion of biomass: fundamentals, technologies, and primary measures for emission reduction. *Energy & fuels*, 17(6):1510–1521, 2003.

[34] European Committee for Standardisation. Industrial thermoprocessing equipment — Part 2: Safety requirements for combustion and fuel handling systems. European Standard EN 746-2:2010, CEN, Brussels, 2010.

UNIVERSITÉ CATHOLIQUE DE LOUVAIN
École polytechnique de Louvain
Rue Archimède, 1 bte L6.11.01, 1348 Louvain-la-Neuve, Belgique | **www.uclouvain.be/epl**